Icarus 233 (2014) 66–82

Contents lists available at ScienceDirect

Icarus

journal homepage: www.elsevier.com/locate/icarus

The dayside ionospheres of Mars and Venus: Comparing a one-dimensional photochemical model with MaRS (Mars Express) and VeRa (Venus Express) observations

Kerstin Peter [a,*], Martin Pätzold [a], Gregorio Molina-Cuberos [b], Olivier Witasse [c], F. González-Galindo [d], Paul Withers [e], Michael K. Bird [a,h], Bernd Häusler [f], David P. Hinson [g], Silvia Tellmann [a], G. Leonard Tyler [g]

[a] *Rheinisches Institut für Umweltforschung an der Universität zu Köln, Abt. Planetenforschung, Köln, Germany*
[b] *Universidad de Murcia, Murcia, Spain*
[c] *Research and Scientific Support Department of ESA, ESTEC, Noordwijk, The Netherlands*
[d] *Instituto de Astrofísica de Andalucía, CSIC, Granada, Spain*
[e] *Boston University, Boston, MA 02215, USA*
[f] *Universität der Bundeswehr München, Neubiberg, Germany*
[g] *Stanford University, Stanford, CA 94305, USA*
[h] *Argelander-Institut für Astronomie, Universität Bonn, Germany*

ARTICLE INFO

Article history:
Received 22 August 2013
Revised 25 November 2013
Accepted 24 January 2014
Available online 3 February 2014

Keywords:
Mars
Venus
Ionosphere

ABSTRACT

The electron density distributions of the lower ionospheres of Mars and Venus are mainly dependent on the solar X-ray and EUV flux and the solar zenith angle. The influence of an increasing solar flux is clearly seen in the increase of the observed peak electron density and total electron content (TEC) of the main ionospheric layers. The model "Ionization in Atmospheres" (IonA) was developed to compare ionospheric radio sounding observations, which were performed with the radio science experiments MaRS on Mars Express and VeRa on Venus Express, with simulated electron density profiles of the Mars and Venus ionospheres. This was done for actual observation conditions (solar flux, solar zenith angle, planetary coordinates) from the bases of the ionospheres to ∼160 km altitude. IonA uses models of the neutral atmospheres at ionospheric altitudes (Mars Climate Database (MCD) v4.3 for Mars; VenusGRAM/VIRA for Venus) and solar flux information in the 0.5–95 nm wavelength range (X-ray to EUV) from the SOLAR2000 data base. The comparison between the observed electron density profiles and the IonA profiles for Mars, simulated for a selected MCD scenario (background atmosphere), shows that the general behavior of the Mars ionosphere is reproduced by all scenarios. The MCD "low solar flux/clear atmosphere" and "low solar flux/MY24" scenarios agree best (on average) with the MaRS set of observations, although the actual Mars atmosphere seemed to be still slightly colder at ionospheric altitudes.

For Venus, the VenusGRAM model, based on VIRA, is too limited to be used for the IonA simulation of electron density profiles. The behavior of the V2 peak electron density and TEC as a function of solar zenith angle are in general reproduced, but the peak densities and the TEC are either over- or underestimated for low or high solar EUV fluxes, respectively. The simulated V2 peak altitudes are systematically underestimated by 5 km on average for solar zenith angles less than 45° and the peak altitudes rise for zenith angles larger than 60°. The latter is the opposite of the observed behavior. The explanation is that VIRA and VenusGRAM are valid only for high solar activity, although there is also very poor agreement with VeRa observations from the recent solar cycle, in which the solar activity increases to high values. The disagreement between the observation and simulation of the Venus electron density profiles proves, that the true encountered Venus atmosphere at ionospheric altitudes was denser but locally cooler than predicted by VIRA.

1. Introduction and background

The properties of planetary ionospheres are accessible to spacecraft by in situ and remote sensing observations. In situ

---

* Corresponding author.
E-mail address: kerstin.peter@uni-koeln.de (K. Peter).

http://dx.doi.org/10.1016/j.icarus.2014.01.028

measurements are rigidly constrained in position and time, as they require that a spacecraft flies through the altitude region of interest, which is for Mars and Venus well below 300 km. The orbit of the Pioneer Venus (PVO) spacecraft descended to altitudes as low 190 km during part of its mission, making it possible to determine the ionospheric composition at and above 190 km (Brace and Kliore, 1991). The only available in situ observations of the ionospheric composition and density structure of the Mars ionosphere were obtained during the two Viking Lander descents to the surface (Hanson et al., 1977). The altitude resolution, however, was coarse.

Remote sensing experiments like radio sounding allow a more frequent and global observation at better altitude resolution (Fresnel radius typically on the order of 500 m). Although radio waves are only sensitive to the electron distribution, it is assumed that the observed density is representative for the density of the ionospheric plasma. The specific ionospheric composition, however, cannot be revealed with this technique.

The Mars atmosphere was sounded for the first time in 1965 during the flyby of Mariner 4 with results that were consistent with a CO_2 composition and a millibar surface pressure. Mariner 9 and the Viking orbiters added only a few observations. Subsequently, Mars Global Surveyor (MGS) provided a vast number of observations of the Mars ionosphere (Hinson et al., 1999; Bougher et al., 2004). The MGS ionospheric observations, however, were constrained geometrically by the sun-synchronized and low-altitude orbit, optimized for the imaging experiments. Radio occultations were limited to high planetary northern and southern latitudes above 60°. The low circular orbit of 400 km limited the achievable sensing altitude to below 220–240 km.

The first observations of the electron density distribution in the Venus ionosphere were obtained by the Mariner Stanford Group (1967). Many other US and Soviet missions followed. A large number of ionospheric radio sounding observations was collected by the Orbiter Radio Occultation (ORO) experiment on PVO from 1978 to 1989 (Kliore et al., 1979). Brace and Kliore (1991) and Fox and Kliore (1997) have both written comprehensive reviews of the ionospheric observations, in situ and radio sounding, which cover almost a full solar cycle.

The neutral atmospheres of Mars and Venus consist predominantly of CO_2 (>95%). Both ionospheres are formed by photoionization by solar EUV and X-ray radiation and, as a secondary effect, below 120 km altitude by photoelectron impact ionization. Whereas CO_2 is the primary photoionized species, rapid reactions with atomic oxygen create O_2^+, which is the dominant ion at the lower ionosphere. The Viking Retarding Potential Analyzers established, that the O^+ concentration becomes comparable to O_2^+ at altitudes above about 250 km (Hanson et al., 1977). For Venus, the PVO ion mass spectrometer revealed a dominance of O^+ above O_2^+ above roughly 200 km altitude (Taylor et al., 1980). The general structures of the martian and the venusian ionospheres are very similar. Fig. 1 shows four electron density profiles from the Mars and Venus ionospheres observed by the Mars Express Radio Science Experiment (MaRS) (Pätzold et al., 2009a) and the Venus Express Radio Science Experiment (VeRa) (Häusler et al., 2006), respectively.

The photochemical regions of the two atmospheres are dominated by two main layers: M2[1] at Mars at about 130 km, and V2 at Venus at about 140 km. Second lower layers, at Mars M1, and at Venus V1, form at altitudes of about 115 km and 125 km, respectively. The dominant main layers, M2 and V2, are formed by solar EUV radiation. The M1 and V1 layers are formed in part by (a) solar X-rays and (b) by impact ionization of photoelectrons (see Fox et al., 1996) for Mars and (Fox, 2007) for Venus).

While the M1 layer in the martian ionosphere has always been regarded as a major feature, some reports of Venus ionosphere observations (Cravens et al., 1981; Kliore and Mullen, 1989) do not mention the V1 layer. The V1 layer is mentioned by Kliore et al. (1967), Kliore et al. (1979) and Breus et al. (1985) and once by Cravens et al. (1981) as "a ledge below the main peak". VeRa observations show that the V1 layer is a persistent, stable feature of the daytime ionosphere, clearly controlled by solar radiation (Pätzold et al., 2007).

For Mars, the M2 peak density and altitude are known to be highly variable, depending on solar zenith angle χ and driven by change in the solar flux.

- Day-to-day changes in the peak densities result from periodic changes of the solar EUV, which are particularly prominent during solar maximum (Withers and Mendillo, 2005).
- Eruptions of solar flares can cause an enhancement in the density of the M1 layer of up to 200% (Mendillo et al., 2006; Haider et al., 2009).

Moreover, additional variations, driven by atmospheric phenomena, have been inferred from the MGS database. These include:

- Upward propagating planetary scale waves originating from the lower atmosphere drive oscillations in pressure, temperature and density of the neutral atmosphere at altitudes up to 150 km, thereby inducing variations of the M2 peak altitude (Bougher et al., 2004; Keating et al., 1998; Withers et al., 2003).
- Transport of dust particles to high altitudes by dust storms heats the neutral gas, which expands raising the base of the ionosphere (Keating et al., 1998; Wang and Nielsen, 2003; Liemohn et al., 2012; Witasse et al., 2003).

Variations of the V2 layer are described by Cravens et al. (1981) and Kliore and Mullen (1989)

- peak density variations as a function of solar zenith angle in a manner consistent with the Chapman theory,
- peak altitude variations, but not in accordance with Chapman theory (e.g. remaining essentially constant for solar zenith angle <70°),
- peak density variations depending on solar EUV flux over the solar cycle as expected from the Chapman theory.

Nevertheless, the formation of quiet ionospheric layers at both Mars and Venus during periods without major perturbations seems to be clearly under solar control. A summary of the observed variability of the dayside ionosphere is given for Mars in Withers (2009) and Withers et al. (2012a,b) and for Venus in Brace and Kliore (1991)).

Sporadic formations of layers below M1/V1 (Pätzold et al., 2005, 2009b) are presumably the result of infalling meteoroids. The surface of these objects ablates during their flight through the atmosphere, depositing metal atoms below about 80 km, that eventually become ionized by photoionization, charge exchange with the background ionosphere, and/or meteoric impact ionization (e.g. Pesnell and Grebowsky, 2000; Molina-Cuberos et al., 2003, 2008; Withers et al., 2008; Whalley and Plane, 2010).

Most of the electron density profiles of both ionospheres show an anomalous accumulation of electrons – referred to here as the

---

[1] Rishbeth and Mendillo (2004) started to call the layers of the Mars ionosphere M1 and M2 for the lower and main layer, respectively. There are authors who name the martian layers E and F1 as in the Earth ionosphere to indicate a similar formation process (Bauer and Hantsch, 1989; Bougher et al., 2001; Fox and Yeager, 2006; Haider et al., 2009; Mahajan et al., 2009). This notation, however, may lead to confusion, in particular when comparing ionospheres from the terrestrial planets. In the following, the system from Rishbeth and Mendillo (2004) is adopted and expanded to Venus to call the lower and main layer V1 and V2, respectively.

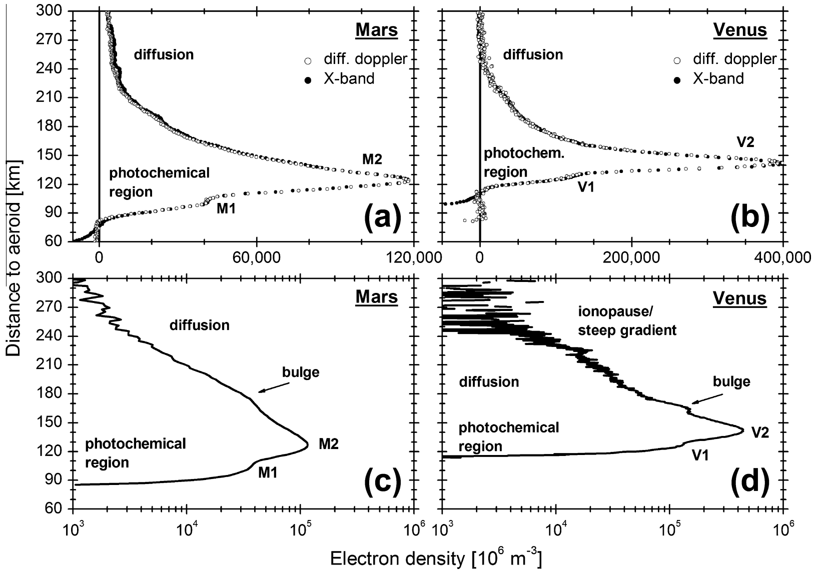

Fig. 1. Electron density profiles from the (a) Mars ionosphere observed with MaRS on 2006 DoY 054 for a solar zenith angle of 52.7°, local solar time of 15.2 h and integrated solar flux $\Phi_{SUM} = 2.0 \cdot 10^{14}\ s^{-1}\ m^{-2}$; (b) Venus ionosphere observed with VeRa on 2008 DoY 17 EGR for a solar zenith angle of 42.7°, local time of 14.6 h and $\Phi_{SUM} = 9.4 \cdot 10^{14}\ s^{-1}\ m^{-2}$. Black circles indicate electron densities derived from a single X-band observations; white circles indicate profiles derived from the differential Doppler. Semi-logarithmic plots of the (c) Mars ionosphere from 2006 DoY 50 diff. Doppler at a solar zenith angle of 53.0° and $\Phi_{SUM} = 2.0 \cdot 10^{14}\ s^{-1}\ m^{-2}$, containing a bulge located at ~180 km; (d) Venus ionosphere from 2009 DoY 200 diff. Doppler ING for a solar zenith angle of 23.1° and $\Phi_{SUM} = 9.3 \cdot 10^{14}\ s^{-1}\ m^{-2}$ with a pronounced bulge and ionopause.

"bulge" – in the region above the main peaks. The genesis of the "bulge" is unknown. One possibility in discussion is a change of electron temperature at about 150–170 km altitude (Fox and Yeager, 2006).

The often sharp outer boundary of the ionosphere, the ionopause, was first detected in the Venus ionosphere by the PVO spacecraft (see summarized results in Brace and Kliore, 1991). Many definitions are in use for this phenomenon, due to the large variety of instruments on board the spacecraft. One definition of the ionopause is the altitude at which a pressure balance exists between the dynamical solar wind and the ionospheric plasma (Schunk and Nagy, 2009). A martian ionopause is also observed under certain atmospheric and solar wind conditions (Peter et al., 2008; Duru et al., 2009). At both Mars and Venus, the ionopause is identified in electron density profiles as a strong negative electron density gradient that continues to the noise level within an increase in altitude of only a few tens of kilometers.

There are a number of models for the Mars and Venus ionosphere: 1-dimensional models which assume photo-chemical equilibrium without transport processes (e.g. Cravens et al., 1981) for Venus and Martinis et al., 2003 for Mars), where the electron density is computed independently for each altitude, 1D models including vertical transport (Fox, 2004; Fox and Yeager, 2006; Mendillo et al., 2011) for Mars and Fox and Sung, 2001 for Venus) where the coupling of the neutral atmospheric layers below and above must be considered. Multi-dimensional models with and without included magnetic field behavior and the actual modeling situation for Mars and Venus are summarized in Bougher et al. (2008).

IonA (Ionization in Atmospheres) is a one-dimensional photochemical model of the martian and venusian ionospheres. Databases of the solar flux (SOLAR2000) and neutral atmosphere (Mars Climate Database (MCD) for Mars and VenusGRAM for Venus) from 0 to 250 km altitude form the basis for the ionospheric calculations. Included effects are the primary ionization of the neutral atmosphere by solar radiation and secondary ionization by a parameterized electron impact ionization. Dissociative recombination of O_2^+ is the included loss process for the generated ions. No transport effects are included, which limits the usable altitude range of the model from the bottom of the ionosphere up to ~160 km altitude. Due to the included databases, external conditions can be easily changed in IonA (e.g. changing solar flux by solar cycle/zenith angle or the neutral atmosphere at a certain longitudinal/latitudinal position of the planet). This allows a flexible modeling of the long MaRS and VeRa observation periods with their changing external conditions. Another advantage of IonA is the short model run time of a few minutes per ionospheric profile. The large variability of the ionosphere (shown by Withers et al., 2012a for Mars), features as the bulge or meteor layers, can be categorized by comparing the whole set of observations with the IonA model results for the correspondent observing parameters. The differences and similarities between observation and model give insight into the formation processes capable or not of forming certain features of the planetary ionospheres. The applicability of IonA to Mars and Venus profiles allows a later use in comparative planetology.

Here we give a first report on the modeling of the Mars and Venus dayside ionospheres by the IonA model for a direct comparison with the observed MaRS and VeRa ionospheric profiles for the core parameters of the ionosphere: altitude, electron density and width of the M2 and V2 main peak and the total electron content of the profile. Following this introduction, Section 2 provides a description of the full observational database and the data subset selected for this paper. Sections 3 and 4 respectively, provide an introduction to the IonA model and a description of the parameters and proxies. Results are discussed in Section 5, followed by the conclusions in Section 6.

2. MaRS and VeRa: observations of the Mars and Venus ionospheres

The radio science experiments MaRS (Pätzold et al., 2004, 2009a), on board the spacecraft Mars Express (MEX), and VeRa, (Häusler et al., 2006) on board Venus Express (VEX), have been in operation in the Mars and Venus orbits since 2004 and 2006, respectively. Both, Mars Express and Venus Express, employ coherent radio signals, operating at frequencies at 8.4 GHz (X-band) and 2.2 GHz (S-band) for the sounding of the respective planetary atmospheres/ionospheres. To date, each of these experiments has obtained more than 600 radio occultation profiles of temperature, pressure, neutral density, and electron density of the day- and night-side (partly published in Withers et al. (2012b)) atmospheres and ionospheres of their planet from ingress (ING) and egress (EGR) – VeRa only – occultations. The MaRS and VeRa daytime data sets with available X- and S-band recordings for the complete ionosphere and $\chi < 85°$ contain 358 observations of the ionosphere for Mars (2004–2011) and 89 ionospheric profiles (2006–2012) for Venus.

Fig. 1a and b shows electron density profiles $n_{e,X}$ obtained from the single X-band frequency data and electron density profiles $n_{e,D}$ calculated from the dual-frequency data. The differential frequency residuals (a.k.a. differential Doppler) are computed from the individual S-band and X-band received radio carrier frequency shifts (see Pätzold et al., 2004)

$$\delta f = \Delta f_S - 3/11 \Delta f_X \tag{2.1}$$

and for the general method (Fjeldbo et al., 1971) where Δf_S and Δf_X contain contributions from the free-space line-of-sight. The X- and S-band carrier frequencies are coherently generated with a constant frequency ratio of 11/3. In other words, terms directly proportional to the carrier frequency, e.g. velocity components, resulting from spacecraft (S/C) or ground station (GS) motion along the line-of-sight are eliminated when calculating the differential frequency residual δf using (2.1). That is, δf can be treated as an observable in the computation of electron density profiles without disturbances by spacecraft motion. The concept of differential Doppler breaks down for altitudes below 80 km, when the propagation of both radio waves is dominated by refraction in the neutral atmosphere and is independent of frequency.

The differential Doppler does not contain S/C or GS motion. It is essentially equivalent to a one-way S-band downlink and more sensitive to the effects of the plasma along the radio ray path, e.g. within the terrestrial ionosphere and/or in interplanetary space, than the X-band frequency. Comparing the electron density profiles derived from differential Doppler and X-band, it is possible to separate the effects of plasma along the radio ray path from those due to motion.

This work makes use of a combination of electron density profiles derived from differential Doppler and X-band data by (i) selecting a "quiet" subset ($n_{e,X}$ and $n_{e,D}$ data for each observation) from the database and (ii) selecting either the $n_{e,X}$ or $n_{e,D}$ profile from the "quiet" data, depending on the average noise level $\sigma_{\text{noise,av}}$, for further investigation.

(i) The quiet profiles comprise those which are unaffected by large-scale plasma disturbances and unusual S/C or GS motion. The status of the ionospheric profiles was tested by the following procedure: Each electron density profile is smoothed by ten consecutive iterations of a short window moving average (for the status test only) in order to reduce the small scale noise:

$$n_{e,\text{av}}(h_i) = \frac{2n_e(h_i) + \sum_{j\neq 0, j=-2}^{2} \frac{0.5abs(h_{i-1}-h_{i+1})}{abs(h_{i+j}-h_i)} n_e(h_{i+j})}{2 + \sum_{j\neq 0, j=-2}^{2} \frac{0.5abs(h_{i-1}-h_{i+1})}{abs(h_{i+j}-h_i)}} \tag{2.2}$$

where $n_{e,\text{av}}(h_i)$ is the smoothed electron density at altitude h_i. The described procedure suppresses most of the small scale noise and leaves the long scale disturbances caused by unusual S/C or GS motion and interstellar plasma. The smoothed electron density above the ionopause is mostly undisturbed by planetary plasma and therefore yields a good estimate for the intensity level of external disturbances. All average profiles with a standard deviation $\sigma_{\text{noise,av}} < 1 \cdot 10^9\ \text{m}^{-3}$ for Mars and $< 6 \cdot 10^9\ \text{m}^{-3}$ for Venus are labeled as "quiet" (exact description of σ_{noise} calculation below).

(ii) Two electron density profiles are derived for each MaRS and VeRa observation: one on the basis of the differential Doppler $n_{e,D}$ and one on the basis of the single X-band carrier frequency $n_{e,X}$. The standard deviations $\sigma_{\text{noise,av,X}}(n_{e,X})$ and $\sigma_{\text{noise,av,D}}(n_{e,D})$ (see below) of the averaged electron density above the planetary ionopause are computed and the profile with the lesser $\sigma_{\text{noise,av}}$ is selected for further analysis. This results in an database consisting of either the $n_{e,D}$ or the $n_{e,X}$ profile for an individual MaRS/VeRa observation. Fig. 1c and d are examples of "quiet" MaRS and VeRa electron density profiles of the Mars and Venus ionospheres.

The number of complete MaRS and VeRa electron density profiles of the dayside ionosphere (solar zenith angle <85°), with available X- and S-band recordings, and an altitude extend above 6400 km above the planetary center (Venus only) reduces with the described procedure to 250 ionospheric profiles for Mars and 84 profiles for Venus.

σ_{noise} is calculated from the electron density above the local aeroid altitude + 800 km for Mars and 6051.8 + 400 km for Venus. If no 50 data points are available above this border, σ_{noise} is calculated from either the electron density above the ionopause or from the highest 50 data points of the profile, detrended with a linear fit.

3. The 1D photochemical IonA model

IonA (Ionization in Atmospheres) is a fast and flexible 1D photochemical software package for simulating the formation of planetary ionospheres up to ~160 km altitude. It is based on models of planetary background neutral atmospheres (available from the planetary surface of up to 250 km altitude): the Mars Climate Data Base (Forget et al., 1999) for Mars and the VenusGRAM model, based on Kliore et al. (1985) for Venus. The background neutral atmosphere is ionized by solar radiation flux data (provided by SOLAR2000 Tobiska et al., 2000) to form the two major layers of the lower ionosphere. The geographic location and time of the observed ionospheric structure around 130 km altitude above the aeroid defines the planetary coordinates, solar zenith angle, local time, solar longitude, and (Mars only) potential dust scenarios for which the neutral atmosphere models and solar flux data are applicable. The aeroid altitudes for Mars are provided by the *heights. F* routine included in the MCD v4.3, which is based on the MGM 1025 spherical harmonics gravity field (an update of the Goddard Mars Model 2B (Lemoine et al., 2001) in combination with the IAU2000 rotation model and cartographic frame (Seidelmann et al., 2002). For Venus a constant aeroid radius of 6051.8 km is assumed. The capability of modeling the ionosphere for the observing parameters given by MaRS and VeRa enables a direct comparison between the observed and the modeled structures. Due to the limited chemistry (the only included loss process is the dissociative recombination of O_2^+) and the lack of included transportation effects, the IonA model is valid below the transport region/bulge feature (app. 160 km altitude).

3.1. Models of neutral background atmospheres

The MCD v4.3 includes vertical profiles of pressure, temperature and concentrations for the species CO_2, O_3, O, N_2, H_2O and Ar (Lewis et al., 1999; Millour et al., 2011). Number densities are computed from the ideal gas law. The MCD distinguishes 8 scenar-

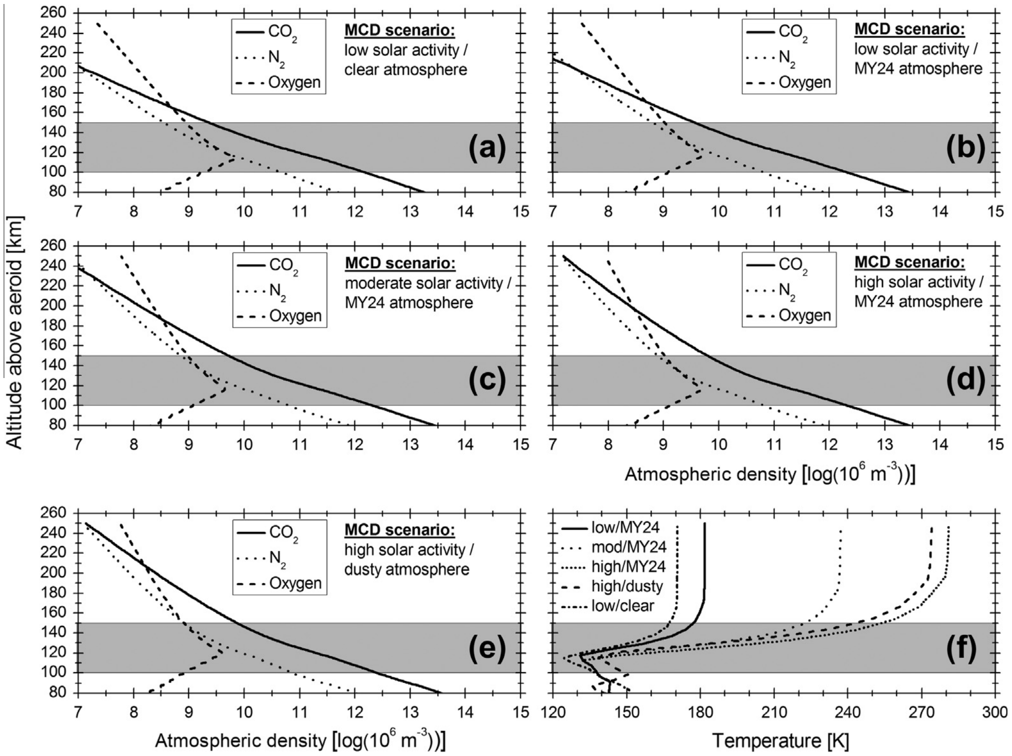

Fig. 2. CO_2, N_2, O number density and temperature profiles for five of the eight available MCD scenarios for 2006 DoY 50, for a solar longitude $L_s = 14.29°$, planetary longitude = 206.01°, latitude = 37.78°, local time = 15.1 h. The shaded area indicates the formation altitude range of the Mars ionosphere.

ios representing the atmospheric variability with dust load and with the solar cycle. The 5 scenarios used in this study are illustrated in Fig. 2: Three scenarios corresponding to Mars Year (MY) 24, for which the dust load was derived from observations by Mars Global Surveyor (MGS) from 1999 to 2001. Pressure and temperature profiles are available for low solar activity with the 10.7 cm radio flux proxy F10.7 ≈ 70 at Earth (called *low/MY24* for the MY24 atmosphere and low solar activity in this paper), moderate solar activity with F10.7 ≈ 130 at Earth (*mod/MY24*), and high solar activity (*high/MY24*) with F10.7 ≈ 200 at Earth. In fact, no F10.7 index or any other proxy index was used, when building the different EUV scenarios for the MCD. The F10.7 values are provided as a reasonable description of the solar flux used in the simulations of the MCD. The MCD scenario “cold and clear” is designed for low solar activity and a clear upper atmosphere with low dust content (*low/clear*); the “warm” scenario for high solar activity and high dust content (*high/dusty*). The 3 MCD “dust storm” scenarios are not further investigated in this paper.

The neutral atmosphere of Venus is described by the VenusGRAM model,[2] which is based on the Venus International Reference Atmosphere (VIRA) (Kliore et al., 1985). Number density, pressure, and temperature profiles can be derived as a function of altitude from 0 to 250 km, latitude, local time and solar zenith angle for the species CO_2, N_2, O, CO, He, N and H. VenusGRAM interpolates between data points for a given solar zenith angle, local time and planetary coordinates. In contrast to the MCD, VenusGRAM has no built in solar flux dependence and no further correction is done to fit the provided data to the observing conditions. The VIRA model tabulates density and temperature values for a fixed value of F10.7 ≈ 150. The F10.7 index used for VIRA was an 8-day average of 10.7 cm solar flux at one astronomical unit distance in solar flux units of 1 SFU = 10^{-22} W m^{-2} Hz^{-1} (Keating et al., 1985).

3.2. The solar flux

The solar photon flux (photons/(s m^2 $\Delta\lambda$)) considered by IonA is taken from the SOLAR2000 model version v2.37 (Tobiska et al., 2000), denoted VUV2002 FUV-UV,[3] which provides historical, nowcast and forecast solar flux data and proxies for Earth with a historical data resolution of one averaged spectral data set per day. The spectral resolution of the data is 1 nm with additional solar spectral lines from the available 39 wavelength bins in the range from 0.5 to 95 nm (because the ionization potential of CO_2 with 13.77 eV requires photons <90.04 nm). As the solar flux output of the Sun is not isotropic, a correction of the SOLAR2000 Earth solar flux in distance and time must be performed for each MaRS or VeRa observation. The percentual difference between the integrated solar flux from 0.5 to 95 nm (see Section 4.2) $\Phi_{\mathrm{SUM,dist}}$, corrected for planetary distance, and $\Phi_{\mathrm{SUM,dist+time}}$, corrected for planetary distance and time is $(\Phi_{\mathrm{SUM,dist}} - \Phi_{\mathrm{SUM,dist+time}})/\Phi_{\mathrm{SUM,dist+time}} = \Phi_{\mathrm{diff}} = (-0.7 \pm 3.6\%)$, where the given error is the standard deviation of Φ_{diff}, where the data set used consists of all MaRS data in this paper. The SOLAR2000 model provides the solar flux for Earth Φ_{Earth}. The solar flux for the IonA calculation Φ_{planet} is calculated for the planetary position at time T_{planet}, the time when the radio sounding observations occur at the planet. T_{planet} defines $T_{\mathrm{Sun,rot}}$, the time needed by the Sun to rotate from the Earth position towards the planet position at T_{planet}. $T_{\mathrm{Sun,rot}}$ can be positive or negative, depending on the position of the Earth ahead of or behind the planet. It is calculated with the Space Geometry Information System SPICE[4] in an iterative procedure, where the planet is fixed and the position of the Earth is varied, until $T_{\mathrm{Earth}} + T_{\mathrm{Sun,rot}} = T_{\mathrm{planet}}$, The solar flux at Earth $\Phi_{\mathrm{Earth}}(T_{\mathrm{Earth}})$ with $T_{\mathrm{Earth}} = T_{\mathrm{planet}} - T_{\mathrm{Sun,rot}}$ is extracted from SOLAR2000 and corrected for the actual planetary

---

[2] http://see.msfc.nasa.gov/tte/VenusGRAM.pdf.

[3] Recommended by K. Tobiska (personal communication), because it includes the variability in the FUV range of the solar spectrum.

[4] naif.jpl.nasa.gov/naif/.

distance

$$\Phi_{\mathrm{planet}}(T_{\mathrm{planet}}) = \Phi_{\mathrm{Earth}}(T_{\mathrm{Earth}})\frac{R^2_{\mathrm{Sun,Earth}}(T_{\mathrm{Earth}})}{R^2_{\mathrm{Sun,planet}}(T_{\mathrm{planet}})} \tag{3.1}$$

by taking into account the respective Sun–Earth distance $R_{\mathrm{Sun,Earth}}$ (T_{Earth}) and Sun–planet distance $R_{\mathrm{Sun,planet}}(T_{\mathrm{planet}})$.

Fig. 3 compares the SOLAR2000 integrated solar flux in the spectral range of 0.5–95 nm from 2004 to the end of 2012 for Earth with the corrected fluxes for Mars and Venus.

3.3. Photochemical reaction scheme

The electron production is calculated from the single and double ionization of the neutral atmospheric species by solar radiation and from secondary ionization by photoelectron impact. The loss of solar photons along the path s is obtained from the Lambert–Beer-law

$$\Phi(s,\lambda) = \Phi^{\infty}(\lambda)e^{-\tau(s,\lambda)} \tag{3.2}$$

where $\Phi(s, \lambda)$ is the photon flux at wavelength λ and path length s, $\phi^{\infty}(\lambda)$ is the incoming photon flux at the top of the atmosphere.

The optical depth $\tau_i(h,\lambda,\chi)$ at altitude h, wavelength λ, and solar zenith angle χ for the molecular or atomic species i is

$$\tau_i(h,\lambda,\chi) = \sigma_{\mathrm{absorb},i}(\lambda)\int_h^{\infty} n_i(h)\cdot Ch_i(h,\chi)dh \tag{3.3}$$

where $n_i(h)$ is the neutral number density at altitude h, $\sigma_{\mathrm{absorb},i}(\lambda)$ is the absorption cross section of species i at wavelength λ and $Ch_i(h, \chi)$ is the Chapman function for grazing incidence angle (Smith and Smith, 1972) for each species i. Values of the absorption and ionization cross sections are from Schunk and Nagy (2009) and for the wavelength range 0.5–5 nm from Avakyan et al. (1998).

The electron production rate $P_i(h, \chi)$ as a function of altitude h and solar zenith angle χ for the species i is

$$P_i(h,\chi) = n_i(h)\int_{\lambda 1}^{\lambda 2} \phi^{\infty}(\lambda)e^{-\tau(h,\lambda,\chi)}\sigma_{\mathrm{ioniz},i}(\lambda)d\lambda \tag{3.4}$$

$$P_t(h,\chi) = \sum_i P_i(h,\chi) \tag{3.5}$$

where $\sigma_{\mathrm{ioniz},i}$ is the ionization cross section for the species i, $\lambda_1 = 0.5$ nm and $\lambda_2 = 95.0$ nm the lower and upper solar radiation wavelengths and $P_t(h, \chi)$ is the total electron production rate summed over all species included in the model: CO_2, N_2 and O (Fig. 4).

At Mars, the in situ observations of the retarding potential analyzers on the Viking 1 and 2 Landers found a peak ion concentration around 130 km altitude consisting of ~90% O_2^+ and 10% CO_2^+ (Hanson et al., 1977), which was reproduced by models (Fox, 2004) with a slightly higher CO_2^+/O_2^+ peak ratio. At Venus, the PVO ion mass spectrometer (OIMS) found, that the lower ionosphere is dominated by O_2^+ down to the spacecraft periapsis of 160 km (Taylor et al., 1980). Model results of the lower ionosphere for low and high solar activity show an O_2^+/electron ratio of >90% at the ionospheric main peak (Fox and Sung, 2001). Main reasons for the large amount of ionospheric O_2^+ are the rapid reactions at rate α_i, (reaction rates for room temperature), which convert the ionized CO_2^+ into O_2^+ (Schunk and Nagy, 2009):

$$CO_2^+ + O \rightarrow O_2^+ + CO \quad \alpha_1 = 1.64\cdot 10^{-16}\ \mathrm{m^3\ s^{-1}}$$

$$CO_2^+ + O \rightarrow O^+ + CO_2 \quad \alpha_2 = 9.6\cdot 10^{-17}\ \mathrm{m^3\ s^{-1}}$$

$$O^+ + CO_2 \rightarrow O_2^+ + CO \quad \alpha_3 = 1.1\cdot 10^{-15}\ \mathrm{m^3\ s^{-1}}$$

The large percentage of O_2^+ in the martian and venusian ionospheres around the main peak makes it possible to simplify the atmospheric chemistry of the IonA model by assuming that every ion produced by (3.4) instantly becomes an O_2^+ ion and that the dissociative recombination of O_2^+

$$O_2^+ + e^- \rightarrow O + O \tag{3.6}$$

is the only loss process for electrons at the rate

$$\alpha_{O_2^+} = 2.4\cdot 10^{-7}\left(\frac{300}{T_e}\right)^{0.7}\cdot 10^{-6}\ \mathrm{m^3\ s^{-1}} \tag{3.7}$$

where T_e is the electron temperature (Schunk and Nagy, 2009).

Assuming that $T_e = T_n$ (neutral temperature), given the limited knowledge on the plasma temperatures (Hanson and Mantas, 1988; Witasse and Nagy, 2006), and assuming that the production rate of electrons is equal to the production rate of ions, balancing the loss of electrons by recombination, provides the equation for the steady state electron density

$$n_e(h,\chi) = \sqrt{\frac{P_t(h,\chi)}{\alpha_{O_2^+}}} \tag{3.8}$$

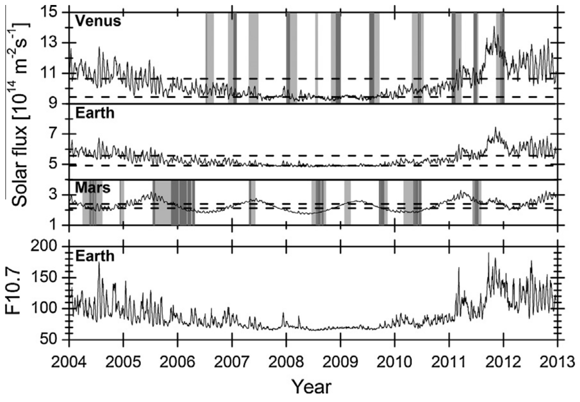

Fig. 3. Integrated solar flux from the SOLAR2000 database from 0.5 to 95 nm for Venus, Earth and Mars. Light gray areas indicate the occultation seasons of Mars Express and Venus Express; dark gray areas indicate the observation subset (dayside) used in this paper. Dashed lines indicate the solar flux boundaries: below the lower line F10.7 < 70; between the lines 70 ⩽ F10.7 ⩽ 100; above upper line F10.7 > 100. Lower panel shows the F10.7 index for Earth from SOLAR2000.

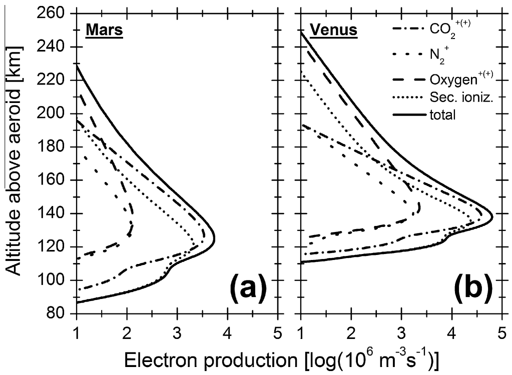

Fig. 4. Electron production calculated for the primary single (+) and double (++) photoionization of neutral CO_2, N_2, and O for (a) Mars 2006 DoY 50, χ = 53.0°, and (b) Venus 2009 DoY 200 ingress, χ = 23.1°. Photoionization of CO_2 dominates below 180 km for Mars, but the ionization of O starts to dominate above this altitude. Secondary ionization dominates below 120 km. For Venus, the ionization of O starts to dominate above 170 km altitude and secondary ionization dominates below 130 km. The solid line is the total number of electrons produced by primary and secondary ionization.

Secondary electron production by electron impact is estimated from the primary electron production by making use of the *W*-value approach (Wedlund et al., 2011), i.e. that one additional ion–electron pair is created for every *W* electron volts of photon energy exceeding the ionization potential of an atom or molecule. The influence of this effect is illustrated in Fig. 4. Short wavelength solar photons penetrate deepest into the atmospheres of Mars and Venus and, due to their high energies, create a large amount of secondary electrons in the altitude region around the M1 and V1 layers.

4. Parameters and proxies of interest

The MaRS/VeRa ionospheric electron density and the IonA modeled profiles are compared on a global and individual scale. For the global comparison, the main peak electron density, altitude and width and the total electron content of each profile are extracted from observation and model. The influence of the varying solar flux is evaluated on observations and model results by defining solar flux ranges for low, moderate and high solar flux.

4.1. Extraction of the observed and modeled parameters

The following parameters are extracted from the observed quiet profiles and the modeled ionospheric profiles:

- M2/V2 peak electron density $n_{e,max}$. A 3σ noise standard deviation $\sigma_{n,max}$ is applied, where σ_{noise} is calculated from the non-averaged observed data as described in Section 2.
- M2/V2 peak altitude $h_{\max}$. The uncertainties $\sigma_{h,max,low}$ and $\sigma_{h,max,up}$ are defined as the difference between $h_{\max}$ and the upper and lower altitudes where the electron density falls below $n_{e,max} - \sigma_{n,max}$.
- M2/V2 layer width $h_{\text{width}} = h_{\text{width,up}} - h_{\text{width,low}}$, is defined by the difference in altitude at 90% of $n_{e,max}$. The upper and lower bounds on h_{width}, $\sigma_{h,width,up}$ and $\sigma_{h,width,low}$ are defined by

$$\sigma_{h,\text{width,up}} = h(n_e(h_{\text{width,up}}) - \sigma_{n,\max}) - h(n_e(h_{\text{width,low}}) - \sigma_{n,\max}) \quad \text{and}$$
$$\sigma_{h,\text{width,low}} = h(n_e(h_{\text{width,up}}) + \sigma_{n,\max}) - h(n_e(h_{\text{width,low}}) + \sigma_{n,\max}).$$

The full width at half maximum (FWHM) of an ionospheric layer is described by the Chapman relation

$$h_{\text{FWHM}} = 3.6H \tag{4.1}$$

with the neutral scale height *H* (Withers, 2009). The FWHM relation is not used, because a layer width derived from 50% of the main peak electron density would include parts of the bulge and the M1 layer.

- Vertical total electron content (TEC), n_{TEC}, obtained by integrating the electron density profile over the significant altitude range from h_{lower} to h_{upper}

$$n_{\text{TEC}} = \int_{h_{\text{lower}}}^{h_{\text{upper}}} n_e(h)dh \tag{4.2}$$

where h_{upper} is 250 km (above the martian aeroid and above the mean Venus radius of 6051.8 km) for observation and model, and h_{lower} is defined by that altitude where the electron density profile disappears within the noise level (returns to zero for the model) at the bottom of the profile. The upper and lower bounds of n_{TEC}, $\sigma_{\text{TEC,up}}$ and $\sigma_{\text{TEC,low}}$, are computed from (4.2) using $n_e + \sigma_{n,\max}$ and $n_e - \sigma_{n,\max}$, respectively, in the integrand.

4.2. The solar flux proxy Φ_{SUM}

The Mars Climate Database v4.3 provides temperature and density profiles of the neutral atmosphere at ionospheric altitudes for three solar activity scenarios: (i) *low* at an approximate 10.7 cm radio flux proxy of F10.7–70, (ii) *moderate* at an approximate F10.7–130 and (iii) *high* at an approximate F10.7–200. To draw a connection between the input ionizing solar flux used in the IonA modeling process (provided by SOLAR2000) and the MCD scenarios for different solar activity, a solar flux proxy Φ_{SUM} is defined. Limits for low, moderate and high solar flux are defined in reference to the given MCD F10.7 values.

The solar flux proxy

$$\Phi_{\text{SUM}} = \int_{0.5}^{95} \Phi(\lambda)d\lambda \tag{4.3}$$

is obtained from SOLAR2000 for every observed profile by integrating the time- and distance-corrected solar flux from 0.5 to 95 nm (due to the wavelength range used in the IonA model). It will be brought into relation to the solar activity proxy: the F10.7 cm solar radiation flux, which is provided in the MCD documentation as solar activity indicator. For the F10.7 intervals (70 ± 1), (130 ± 1) and (200 ± 1) the corresponding Φ_{SUM} values between January 2004 and December 2011 are averaged to yield solar flux limits $\Phi^{\text{Earth}}_{\text{SUM}}$ at the Earth position. The associated fluxes at Mars and Venus are adjusted by the appropriate mean planetary distances (3.1).

A solar flux value of $\Phi[70]^{\text{Earth}}_{\text{SUM}} = 4.94 \pm 0.05 \cdot 10^{14}\ \text{m}^{-2}\ \text{s}^{-1}$ (335 SOLAR2000 entries) is computed for F10.7 = 70. The error is the standard deviation from the 335 extracted SOLAR2000 entries. The average solar flux and standard deviation for F10.7 = 130 at Earth is $\Phi[130]^{\text{Earth}}_{\text{SUM}} = 6.2 \pm 0.2 \cdot 10^{14}\ \text{m}^{-2}\ \text{s}^{-1}$ (14 entries). No data for F10.7 = 200 ± 1 are available during the selected time interval. Adjusting the flux to Mars gives $\Phi[70]^{\text{Mars}}_{\text{SUM}} \sim 2.13 \cdot 10^{14}\ \text{m}^{-2}\ \text{s}^{-1}$ and $\Phi[130]^{\text{Mars}}_{\text{SUM}} \sim 2.67 \cdot 10^{14}\ \text{m}^{-2}\ \text{s}^{-1}$ and for the Venus average position $\Phi[70]^{\text{Venus}}_{\text{SUM}} \sim 9.44 \cdot 10^{14}\ \text{m}^{-2}\ \text{s}^{-1}$ and $\Phi[70]^{\text{Venus}}_{\text{SUM}} \sim 11.85 \cdot 10^{14}\ \text{m}^{-2}\ \text{s}^{-1}$.

There are only 10 MaRS and 6 VeRa observations for which the solar flux $\Phi^{\text{Planet}}_{\text{SUM}}$ exceeds $\Phi[130]_{\text{SUM}}$. It is therefore appropriate to lower the upper solar flux limit to $\Phi[100]^{\text{Mars}}_{\text{SUM}} = 2.4 \cdot 10^{14}\ \text{m}^{-2}\ \text{s}^{-1}$ for Mars and to $\Phi[100]^{\text{Venus}}_{\text{SUM}} = 10.65 \cdot 10^{14}\ \text{m}^{-2}\ \text{s}^{-1}$ for Venus, which is the average solar flux between $\Phi[70]^{\text{Earth}}_{\text{SUM}}$ and $\Phi[130]^{\text{Earth}}_{\text{SUM}}$, calibrated to the average planetary distances of Mars and Venus. The F10.7 values are used to give an appropriate estimate of the available solar flux Φ^{∞} used in the model calculations (Eq. (3.2)).

Three solar flux intervals are used to distinguish the solar flux levels for both planets: (i) F10.7 < 70 for the lowest solar flux $\Phi_{\text{SUM}} < \Phi[70]_{\text{SUM}}$, (ii) $70 \leqslant \text{F10.7} \leqslant 100$ for moderate solar flux $\Phi[70]_{\text{SUM}} \leqslant \Phi_{\text{SUM}} \leqslant \Phi[100]_{\text{SUM}}$ and F10.7 > 100 for the highest solar flux $\Phi_{\text{SUM}} > \Phi[100]_{\text{SUM}}$.

5. Comparison of observation and model

The straightforward design of the IonA software allows the study of the individual effects of changing solar flux, neutral density and temperature on an ionosphere in photochemical equilibrium. Increasing or decreasing the solar flux enhances or reduces, respectively, the electron density due to more or less available solar ionizing photons and their individual energy distribution. An increase of the atmospheric density around and above the main ionospheric layer increases the altitude of the entire ionospheric profile due to the change in the solar radiation absorption profile. A local change in the neutral scale height around the M/V2 region causes a change in width of the main peak (larger width for larger scale heights). A change in neutral temperature changes the structure of the whole neutral atmosphere by changing its scale height (see Eq. (5.3)). A local increase (decrease) in temperature causes an increase (decrease) of electron density due to a decrease (increase) in the dissociative recombination rate of O_2^+ (Eqs. (3.7) and (3.8)).

5.1. Modeling the Mars ionosphere

Fig. 5 compares the MaRS observation of 2006 Day of Year (DoY) 50 with the IonA model results for the five MCD scenarios. The modeled electron density profiles were computed for the parameters specified by the observation, i.e. solar longitude, planetary location, solar zenith angle and local solar time. Fig. 5a shows the modeled profile using the temperature and neutral density profiles from the *low/clear* MCD scenario, which represents a cold and clear atmosphere. The profiles in Fig. 5b–d are from the *low/MY24*, *mod/MY24* and *high/MY24* scenarios, respectively, Fig. 5e is modeled on the basis of the *high/dusty* MCD scenario. The temperatures of these scenarios represent increasingly warmer atmospheres. The observation agrees well with the cooler atmospheres from the MCD scenarios *low/clear* and *low/MY24* (Fig. 5a and b). The electron density derived from primary ionization is well below the observed density values for the M1 and M2 layers. There is very good agreement between observation and model if the secondary ionization effects are considered. The main peak M2 is mainly produced by primary photoionization, as expected (Withers and Mendillo, 2005; Schunk and Nagy, 2009). The secondary ionization is most effective at lower altitudes and dominates the contribution to the M1 layer electron density. The bulge above the M2 main peak in Fig. 5 is not modeled by photoionization and secondary impact ionization and is therefore not seen in any of the other modeled electron density profiles. This indicates that the bulge is not formed by the ionization processes included in IonA. Possible origins are vertical transport and an increase in the electron temperature at this altitude, which change the recombination rate and thus the electron density.

Differences between observation and model increase from Fig. 5c to e. The reason is the very low solar flux at the time of the observation on 2006 DoY 50 (see Fig. 3), which is well represented by the *low/cold* and *low/MY24* MCD scenarios with low solar activity and a cool background atmosphere.

Fig. 6 compares the observed and modeled M2 peak densities for the selected data set. For an ionosphere ideally controlled by solar radiation, the peak density should vary with the solar zenith angle and is usually compared with the Chapman relation

$$n_{e,\max}(\chi) = n_{e,0}(\chi = 0) \cdot \cos^{\varepsilon}\chi \tag{5.1}$$

where $n_{e,\max}(\chi)$ is the peak density at the solar zenith angle χ, $n_{e,0}$ is the peak density for $\chi = 0$ and $\varepsilon = 0.5$ is the exponent for perfect agreement with the Chapman theory. The observed data in Fig. 6a demonstrate the decrease of the main peak electron density with increasing solar zenith angle, as predicted from the Chapman relation. This general behavior is reproduced by IonA for all five MCD scenarios (Fig. 6b–f).

The influence of the changing solar flux on the Mars ionosphere is also shown in Fig. 6a. The MaRS observations are subdivided into the three solar flux intervals discussed in Section 4.2. The Chapman relation (5.1) is fit to the moderate solar flux interval $70 \leqslant \text{F10.7} \leqslant 100$. Most of the M2 densities within the solar flux interval F10.7 < 70 are below the Chapman relation fit (dashed line in Fig. 6a), while most of the M2 densities of interval F10.7 > 100 are above. This illustrates the strong dependence of the M2 peak on the actual solar flux. Fig. 6b compares the observations with models using the *low/clear* MCD scenario. IonA is able to reproduce the behavior of the M2 peak due to the changing solar flux.

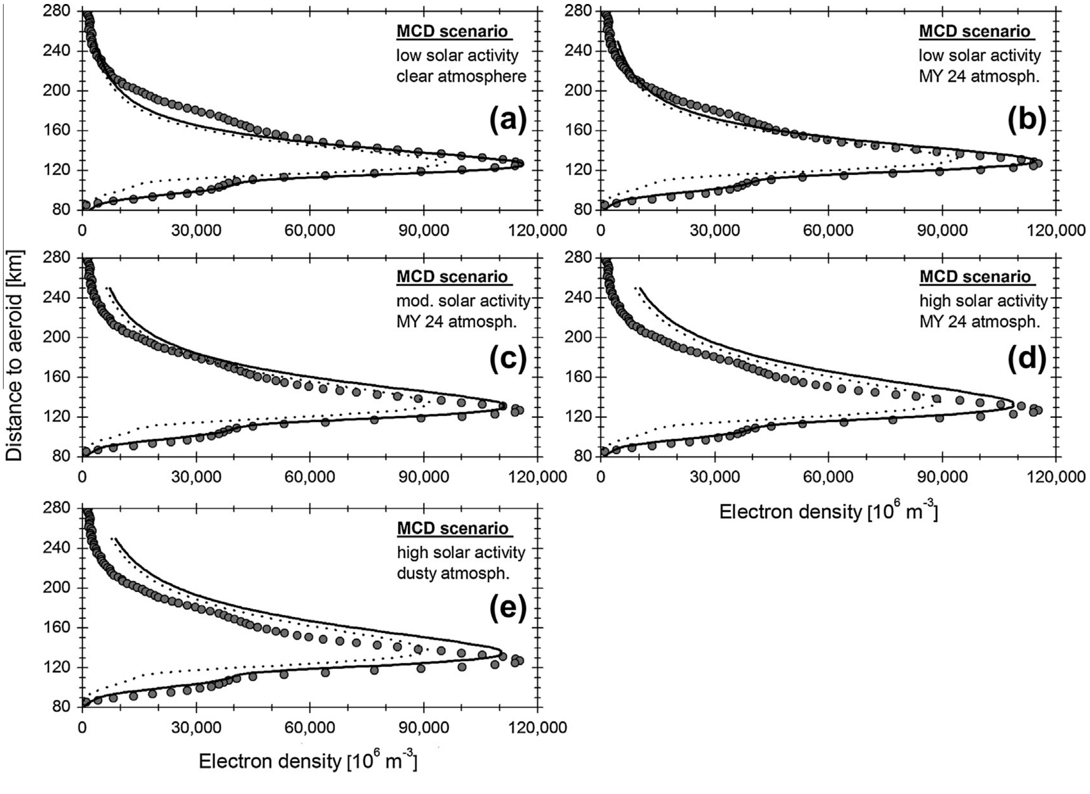

Fig. 5. Comparison between the observed MaRS electron density profile from 2006 DoY 50 for $L_s = 14.3°$, pl. lon. = 206.0°, pl. lat = 37.8°, $\chi = 53.0°$ and $\Phi_{\mathrm{SUM}} = 2.0 \cdot 10^{14}$ s^{-1} m^{-2} (gray dots) and IonA model results for five MCD scenarios. The dotted line is derived from primary photoionization only, the solid line considers additionally the secondary ionization: (a) MCD *low/clear* scenario, (b–d) *low/mod/high MY24* scenarios, respectively, (e) high/dusty scenario. While the model is in good agreement with the observation in panels (a and b), the differences grow larger from (c) to (e). This is expected, because the selected MaRS electron density profile is from a period of low solar activity, represented best by a cool atmosphere, while the models (c–e) represent warmer atmospheres.

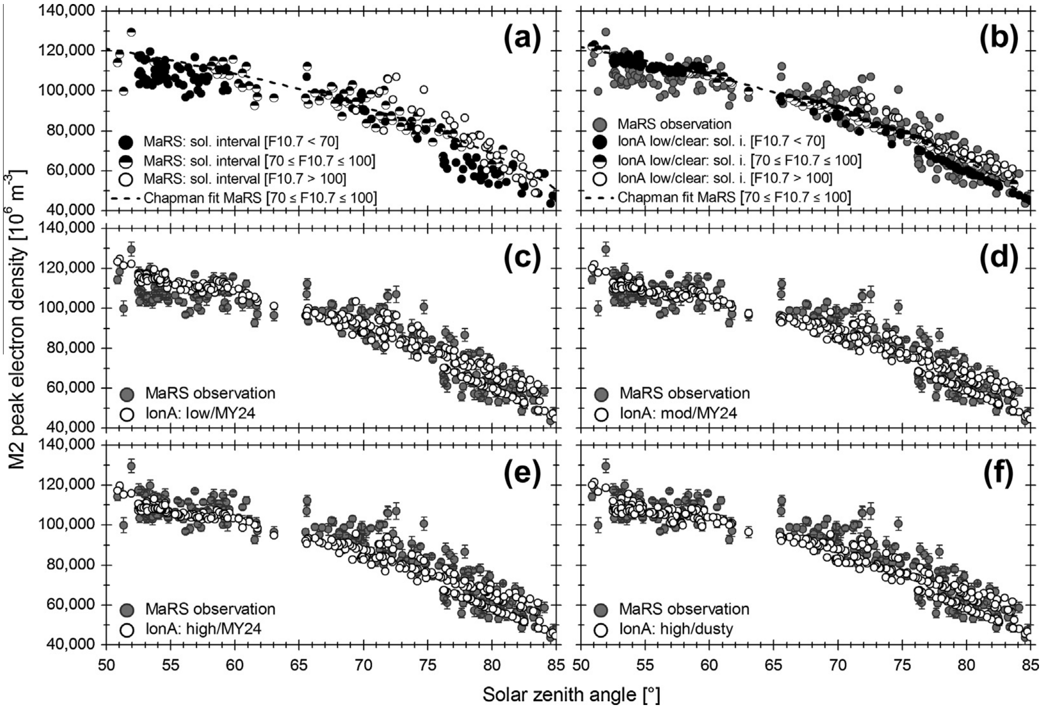

Fig. 6. Observed and modeled peak densities for the M2 layers: (a) observed electron density of the ionospheric M2 main peak. Black circles are observations for a solar flux below $2.13 \cdot 10^{14}\ \mathrm{m^{-2}\ s^{-1}}$ F10.7 < 70, black/white circles are observations for a solar flux between $2.13 \cdot 10^{14}\ \mathrm{m^{-2}\ s^{-1}}$ and $2.4 \cdot 10^{14}\ \mathrm{m^{-2}\ s^{-1}}$ $70 \leqslant$ F10.7 $\leqslant 100$, and white circles for a solar flux above $2.4 \cdot 10^{14}\ \mathrm{m^{-2}\ s^{-1}}$ F10.7 > 100. The Chapman fit (5.1) yields $\varepsilon_{\mathrm{obs}}(70 \leqslant \mathrm{F10.7} \leqslant 100) = 0.437 \pm 0.004$ (dashed line), compared to an ideal value of 0.5; (b) observed data (gray circles) and IonA model results for the MCD *low/clear* scenario. The model values are shown as black circles for F10.7 < 70, black/white circles for $70 \leqslant$ F10.7 $\leqslant 100$, and white circles for F10.7 > 100. The Chapman relation fit for the modeled data yields $\varepsilon_{\mathrm{mod}}(70 \leqslant \mathrm{F10.7} \leqslant 100) = 0.49$; (c–f) comparisons between observations and IonA model results for the MCD *low/MY24*, *mod/MY24*, *high/MY24* and *high/dusty* scenarios, respectively. The temperature of the background neutral atmosphere is increasing from panel (c) to (f).

Considering the electron density of the M2 peak only, it is evident from Fig. 6, that there is no “best” MCD atmospheric scenario. Under the assumption, that a modeled M2 peak electron density “fits” its observation when the residual between observation and model is within the error bars given in Section 4.1, the agreement between observation and all used MCD scenarios lies between 22% and 26% (see Table 5.2). The smaller fluctuations of the modeled peak densities for a certain solar zenith angle interval in comparison to the observations is explained by: (i) observational uncertainties (not included as error bars for the sake of clarity), (ii) model uncertainties caused by missing effects in the SOLAR2000/MCD databases (e.g. missing day-to-day atmospheric or solar flux variability) and the fact that the solar flux used for modeling is only available for the position of the Earth, and (iii) multidimensional and transport effects not included in the 1D photochemical model.

Observed and modeled peak altitudes are compared in Fig. 7. The Chapman relation for the peak altitude is

$$h_{\max}(\chi) = h_0(\chi = 0) - H \cdot \ln(\cos\chi) \tag{5.2}$$

where $h_{\max}(\chi)$ is the peak altitude for the solar zenith angle χ, h_0 is the peak altitude for $\chi = 0$ and the neutral scale height

$$H = \frac{k_B T_n}{mg} \tag{5.3}$$

with the Boltzmann constant k_B, the neutral temperature T_n, the average (homosphere) or molecular/atomic (heterosphere) mass m and g the gravity acceleration. Despite the large variation of the observed M2 peak altitudes in Fig. 7a, a clear altitude/solar zenith angle dependence, as expected from the Chapman theory, is evident. This general trend is reproduced by IonA for all MCD scenarios. The M2 peak altitudes modeled from the temperature and density profiles from the MCD *low/clear* and *low/MY24* scenarios fit best on average (Fig. 7b and c). The modeled peak altitudes for all other (warmer) MCD scenarios are significant higher than the observed peak altitudes (Fig. 7d–f), indicating that the atmosphere at the time of the observation is cooler than predicted on average in these scenarios. Higher temperatures let the atmosphere expand leading to ionospheric layers at higher altitudes. (Forget et al., 2009) found in a comparison of the MCD neutral atmosphere with SPICAM (Spectroscopy for Investigation of Characteristics of the Atmosphere of Mars, an imaging spectrometer for ultraviolet and infrared radiation on Mars Express) (Bertaux et al., 2004) results an overestimate of temperatures in ionospheric altitudes at the nightside of Mars. An improved version of the MCD will include a better description of the cooling produced by the 15 µm emissions of CO_2 and its dependence with the abundance of atomic oxygen (López-Valverde et al., 2011). This cooling term, dominant at the upper mesosphere/lower thermosphere, has been identified as the likely responsible of the overestimation of the temperatures (Forget et al., 2009; González-Galindo et al., 2009).

The change in solar flux during the observation periods from 2004 to the end of 2011 and its impact on the martian ionosphere is seen in Fig. 7a. The observations are divided into the three solar intervals described in Section 4.2. The Chapman relation (5.2) was fit to the observations assigned to the moderate solar flux interval $70 \leqslant$ F10.7 $\leqslant 100$. The influence of the varying solar flux on the Mars ionosphere, already found for the peak electron density (Fig. 6a), is confirmed and reflected in an increase of the peak altitude for increasing values of the solar flux. The same influence of the solar flux is found for the *low/clear* model results in Fig. 7b.

Fig. 8 compares the observed and the modeled M2 layer widths for the selected MCD scenarios. The linear fits in Fig. 8a illustrate the behavior of the M2 width due to the varying solar flux. The fit-slopes are listed in Table 5.1. In an ionosphere, developing in

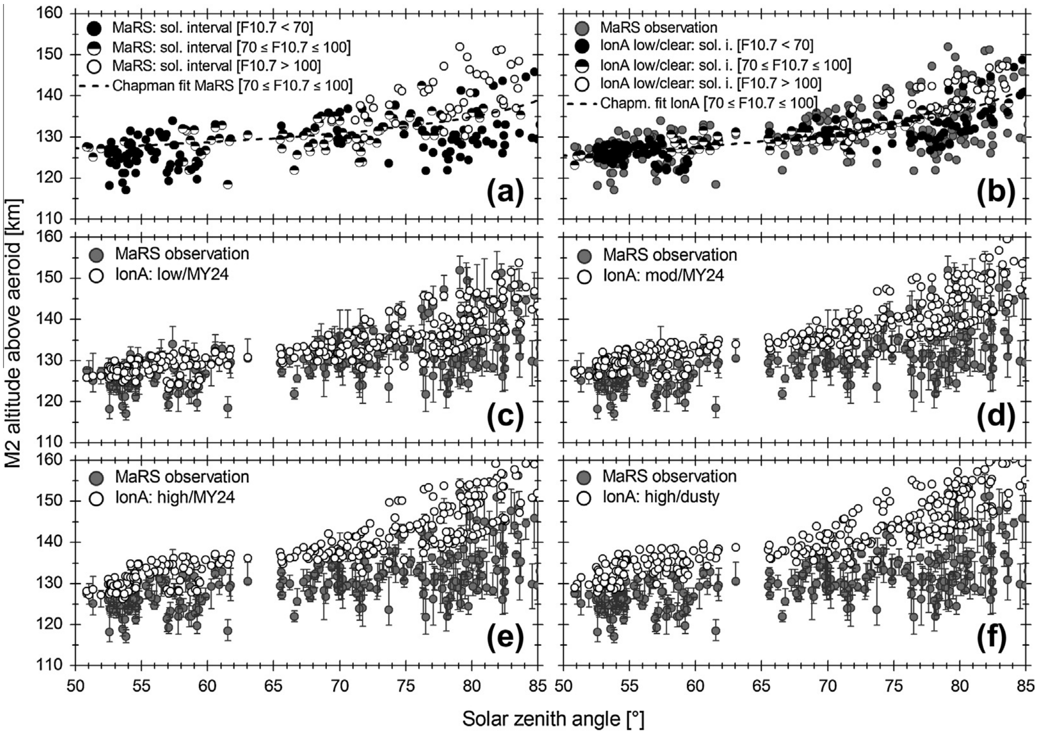

Fig. 7. Observed and modeled altitude of the M2 main peak: (a) observed M2 peak altitudes. Black circles are for the solar flux interval F10.7 < 70, black/white circles for interval $70 \leqslant F10.7 \leqslant 100$ and white circles for solar flux interval F10.7 > 100. The Chapman fit yields $H_{obs}(70 \leqslant F10.7 \leqslant 100) = 5.8 \pm 0.5$ km with assumed errors for the fit of $\sigma_{h,max,av} = (\sigma_{h,max,low} + \sigma_{h,max,low})/2$; (b) observed data (gray circles) and the IonA model results for the MCD low/clear scenario as black circles for interval F10.7 < 70, black/white circles for interval $70 \leqslant F10.7 \leqslant 100$ and white circles for interval F10.7 > 100. The Chapman relation fit (5.2) for the modeled data produces $H_{mod}(70 \leqslant F10.7 \leqslant 100) = 8.3$ km. H is considered without solar zenith angle dependence here, and is only used to indicate the border between low and high solar activity data; (c–f) are the comparison between observation and IonA model results for the MCD *low/MY24*, *mod/MY24*, *high/MY24* and *high/dusty* scenarios.

a single-species atmosphere by monochromatic radiation, with only locally constant H, an increase in M2 width with solar zenith angle can be caused by two effects:

(i) Increasing/decreasing solar flux between ionospheric observations can cause the neutral atmospheric temperature to rise/fall, generating higher/lower scale heights H by an expanding/collapsing atmosphere (Eq. (5.3)).
(ii) The increasing M2 peak altitude for increasing zenith angle (see Fig. 7) may cause the formation of the M2 layer in altitude regions with a higher neutral scale height H.

Fig. 9 shows the Φ_{SUM} vs. χ dependence for the used MaRS observations, grouped into the three solar activity intervals. The resulting fit-slopes are listed in Table 5.1.

There is no increase in M2 width with increasing solar zenith angle for the F10.7 < 70 interval. This indicates, in combination with the decreasing Φ_{SUM} in Fig. 9, that the atmosphere cooled down slightly for the higher zenith angle observations. This would explain the absent M2 width increase for higher zenith angle data.

For the $70 \leqslant F10.7 \leqslant 100$ interval, the M2 width is increasing, as is the solar flux Φ_{SUM} with increasing χ. Therefore the increase in M2 width can be caused by higher neutral scale heights, caused by increasing Φ_{SUM}, and by the increase in M2 peak altitude, causing the main peak to form in regions of higher H.

There is a strong broadening of the M2 layer for decreasing Φ_{SUM} with increasing χ for the F10.7 > 100 interval. This indicates, that the main cause for the M2 broadening is the increase of the M2 altitude into regions containing higher neutral scale heights.

The modeled M2 layer width is very sensitive to the selected MCD scenario (Fig. 8b–f) and therefore to the temperature of the background neutral atmosphere. The width of the ionospheric main peak is much smaller for the *low/clear* and *low/MY24* scenarios than for the warmer scenarios. The modeled M2 width from the warmer MCD scenarios is too broad on average when compared with the observations (see Table 5.2), which is explained by the formation in regions of higher neutral scale heights, which, again, increases the width of the modeled M2 layer. This is again an indication of the overestimation of the temperatures at ionospheric altitudes by the MCD v4.3.

Fig. 10 compares the observed and modeled electron content of the vertical electron density profiles computed from Eq. (4.2). The Chapman theory predicts a direct dependence on the neutral scale height H (Withers, 2009)

$$n_{TEC} \sim 4.13 \frac{n_{e,0}}{\sqrt{Ch(h,\chi)}} H \tag{5.4}$$

The observations in Fig. 10a show a strong solar zenith angle dependence as expected from the relation (5.4). This general trend is reproduced by IonA for all MCD scenarios (Fig. 10b–f). The observed TEC is strongly related with the actual solar flux, which is also found in the model results (Fig. 10b). The modeled TEC values for the *low/clear* and the *low/MY24* scenarios agree best with the observations (see Table 5.2).

5.2. Modeling the Venus ionosphere

IonA uses the VenusGRAM model neutral atmosphere as background for the modeling of the Venus ionosphere. VenusGRAM is available for a fixed F10.7 value of 150 only (see Section 3.1), while most of the VeRa observations were performed during a period of lower solar activity. Fig. 11 compares observed and modeled electron density profiles from the Venus ionosphere. The modeled V2

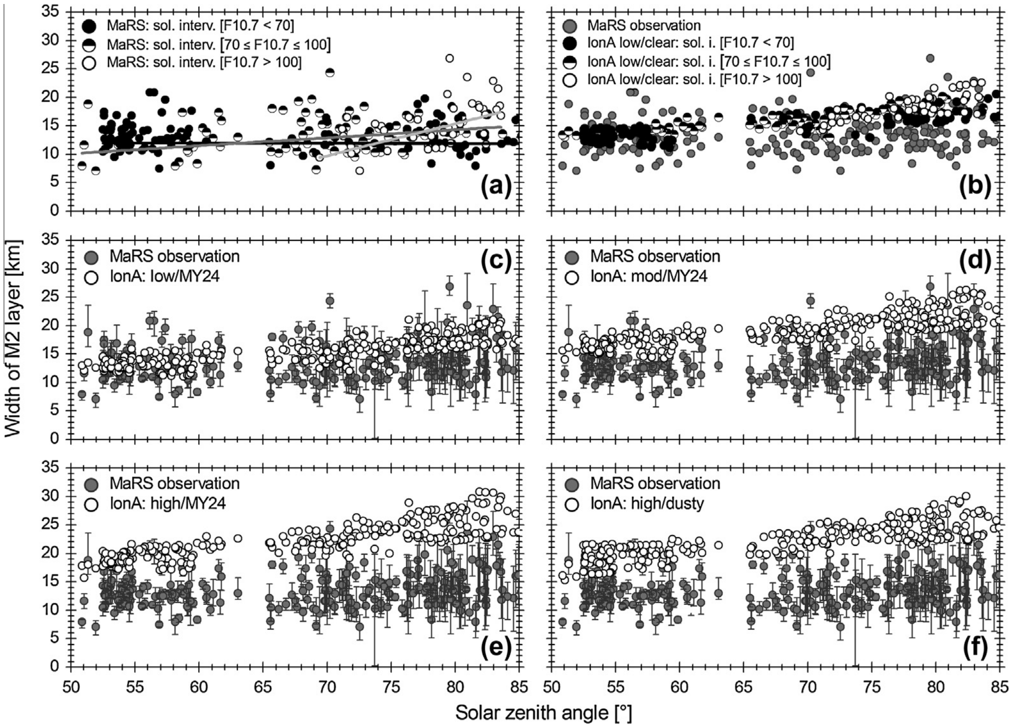

Fig. 8. Width of the M2 main layer: (a) observed M2 widths of the ionospheric main peak. Black circles and black line are for the solar flux interval F10.7 < 70, black/white circles and dark gray line for interval 70 ⩽ F10.7 ⩽ 100 and white circles and light gray line for the solar flux interval F10.7 > 100. The linear fits were conducted with the averaged width errors $\sigma_{h,\mathrm{width,av}} = (\sigma_{h,\mathrm{width,low}} + \sigma_{h,\mathrm{width,low}})/2$; (b) observed data (gray circles) and the IonA model results for the MCD *low/clear* scenario for interval F10.7 < 70 as black circles, black/white circles for interval 70 ⩽ F10.7 ⩽ 100 and white circles for interval F10.7 > 100; (c–f) are the comparison between observation and IonA model results for the MCD *low/MY24*, *mod/MY24*, *high/MY24* and *high/dusty* scenarios.

Table 5.1
Slopes for the linear fits of M2 width vs. solar zenith angle and Φ_{SUM} vs. solar zenith angle. Assumed errors are: $\sigma_{h,\mathrm{width}} = (\sigma_{h,\mathrm{width,low}} + \sigma_{h,\mathrm{width,up}})/2$ for M2 width and $\sigma(\Phi_{\mathrm{SUM}}) = 0.1 \cdot 10^{14}\ \mathrm{m}^{-2}\ \mathrm{s}^{-1}$.

	Slope M2 width vs. χ (km/°)	Slope Φ_{SUM} vs. χ ($\mathrm{s}^{-1}\ \mathrm{m}^{-2}$/°)
F10.7 < 70	0.00 ± 0.02	−0.004 ± 0.001
70 ⩽ F10.7 ⩽ 100	0.14 ± 0.01	0.008 ± 0.001
F10.7 > 100	0.56 ± 0.09	−0.004 ± 0.004

layer is mainly formed by EUV radiation (dotted line in Fig. 11), but underestimates the observed peak electron density usually by 10–30%. Secondary ionization contributes to the observed peak density. The V1 layer is formed by solar X-rays and by secondary ionization predominantly. VeRa observations and the modeled IonA profiles are in good agreement in Fig. 11a and b and although the general shape of the modeled electron density profiles is usually quite similar to the observations, there are significant systematic differences.

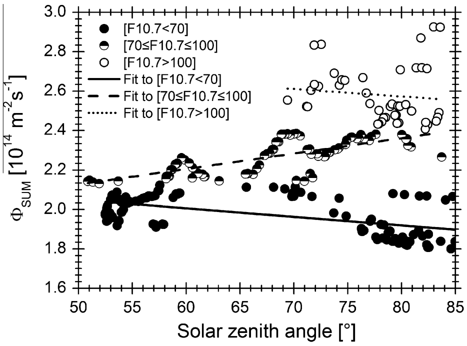

Fig. 9. Integrated solar flux Φ_{SUM} for all used MaRS observations in dependence of the solar zenith angle. For the linear fits, an error of $0.1 \cdot 10^{14}\ \mathrm{s}^{-1}\ \mathrm{m}^{-2}$ is assumed for the integrated solar flux.

Fig. 11c is an example where the modeled electron density overestimates the observed V2 peak density during a time period of low solar flux, Fig. 11 d shows an underestimated V2 peak density for an observation conducted during a higher solar flux period. The electron density profiles in Fig. 11 e and f were observed by VeRa one Venus year apart.

Fig. 12a and b shows the VIRA CO_2 number density and temperature profiles taken from VenusGRAM for the altitude range of 100–250 km. The VenusGRAM model provides temperature and density profiles for a local solar time of 0 h and for a local solar time of 12 h between 100 km and 150 km altitude (no direct zenith angle dependence). Dayside VIRA profiles for solar zenith angles of 15°, 34°, 61° and 90° are provided for the altitude range between 150 km and 250 km (no local time dependence). The transition region between the lower and upper profiles at 150 km is smoothly bridged by VenusGRAM. Although VenusGRAM interpolates and smoothes the profiles from the VIRA database, it returns clearly and significantly a break between profiles generated for solar zenith angles smaller and larger than 61°. This unphysical discontinuity is translated into the modeled profiles. Fig. 12c–f shows the neutral atmospheres and temperatures generated from VenusGRAM for the observations in Fig. 11a–d. For further comparisons between VIRA and VeRa observations see Tellmann et al. (2009).

Fig. 13a shows the observed V2 peak electron density as a function of solar zenith angle. The typical decrease of the peak electron density with increasing solar zenith angle is seen in both observation and model (Fig. 13b). Three populations are apparent: Observations for F10.7 < 70 are more or less from the solar minimum

Table 5.2

Percentage of the IonA model results which "fit" their observation in the described category. A modeled ionospheric main peak electron density $n_{e,\max,\mathrm{mod}}$ fits its associated observation $n_{e,\max,\mathrm{obs}}$, when $n_{e,\max,\mathrm{obs}} - \sigma_{n,\max} \leqslant n_{e,\max,\mathrm{mod}} \leqslant n_{e,\max,\mathrm{obs}} + \sigma_{n,\max}$. The described pattern is adapted for all categories.

MCD scenario	M2 electron density (%)	M2 altitude (%)	M2 width (%)	TEC (%)
Low/clear	23.6	60.4	36.0	44.0
Low/MY24	24.4	50.8	38.8	45.6
Mod/MY24	22.4	22.0	12.8	13.6
High/MY24	25.6	11.6	5.2	6.4
High/dusty	22.4	3.6	4.4	4.4

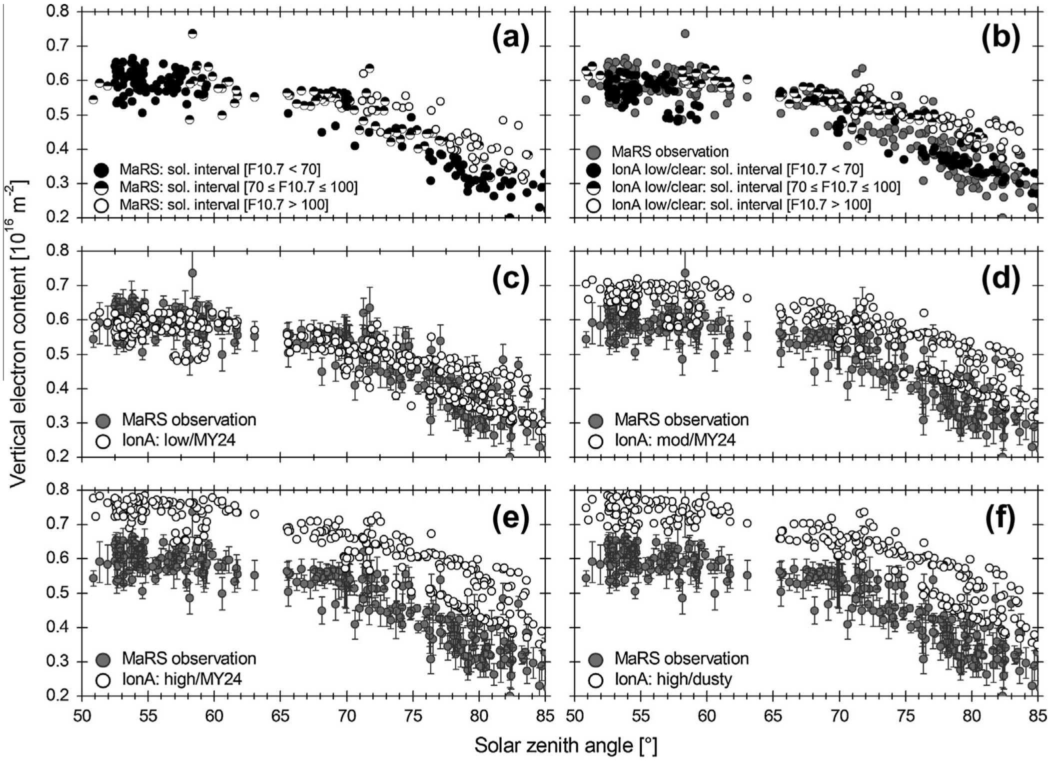

Fig. 10. Comparison of the observed and modeled electron content (TEC) of the Mars ionosphere: (a) observed TEC, integrated from the bottom of the ionosphere up to 250 km altitude. Black circles indicate the solar flux interval F10.7 < 70, black/white circles the flux interval 70 ⩽ F10.7 ⩽ 100 and white circles the interval F10.7 > 100; (b) contains the observed data (gray circles) and the IonA model results for the MCD *low/clear* scenario as black circles for interval F10.7 < 70, black/white circles for interval 70 ⩽ F10.7 ⩽ 100 and white circles for interval F10.7 > 100; (c–f) compare the MaRS observations and IonA model results for the MCD *low/MY24*, *mod/MY24*, *high/MY24* and *high/dusty* scenarios.

activity interval 2008 to 2009 (Fig. 13e). The observations for 70 ⩽ F10.7 ⩽ 100 are from late 2006 to the beginning of 2008 (decline of solar cycle 23) and between 2010 and 2011 (rise of new solar cycle 24). The highest solar activity F10.7 > 100 is found during the rise of the new solar cycle 24 from mid 2011 to 2012. Fig. 13e explains the different populations for F10.7 > 100 of Fig. 13a due to two separated solar flux intervals below and above $11.25 \cdot 10^{14}$ m^2/s.

Fig. 13b compares the observed peak densities with the modeled V2 peak densities. While the general dependence of the observed V2 densities on solar zenith angle and solar flux is reproduced, the detailed situation is more complicated. The modeled V2 peak densities are systematically overestimated for F10.7 < 70, observation and model agree best for 70 ⩽ F10.7 ⩽ 100 and the modeled V2 peak densities are underestimated for F10.7 > 100. While the authors of the VIRA profiles (150–250 km altitude) state a F10.7 value of 150 (high solar activity), the best agreement between observations and model results is however found for solar flux values of 70 ⩽ F10.7 ⩽ 100.

The altitude of the observed V2 peak (Fig. 13c) does not vary strongly for solar zenith angles less than 65°, although some points seem to rise starting at $\chi \geqslant 45°$. The peak altitude tends to decrease down to lower altitudes for $\chi \geqslant 65°$. A similar behavior was seen with PVO (Cravens et al., 1981), which was explained by two competing effects: (i) the rise of the main peak altitude due to an increase of the solar zenith angle (Eq. (5.2)) and (ii) the cooling (collapsing) of the neutral atmosphere towards the terminator ($\chi > 85°$). When the first effect dominates, the V2 peak rises slightly for increasing solar zenith angles. If the second effect dominates, the V2 peak altitude will drop. The observed peak altitude is also obviously independent of the solar flux as there is no strong difference seen between the data in the three solar flux intervals. Kliore and Mullen (1989) with an update in Brace and Kliore (1991) found an average altitude of the V2 peak for solar minimum at 136.8 ± 6.4 km and for solar maximum at 142.2 + 6.3 km. A larger VeRa dataset, containing especially higher solar flux data, is necessary to confirm these results.

The IonA model, however, displays a strong increase of the peak altitude for $\chi \geqslant 61°$, a behavior opposite to the observation (Fig. 13d). The V2 peak altitudes are systematically underestimated for $\chi < 45°$ by 5 km on average when compared with the observations. The reason for this contrary behavior is obviously the limited

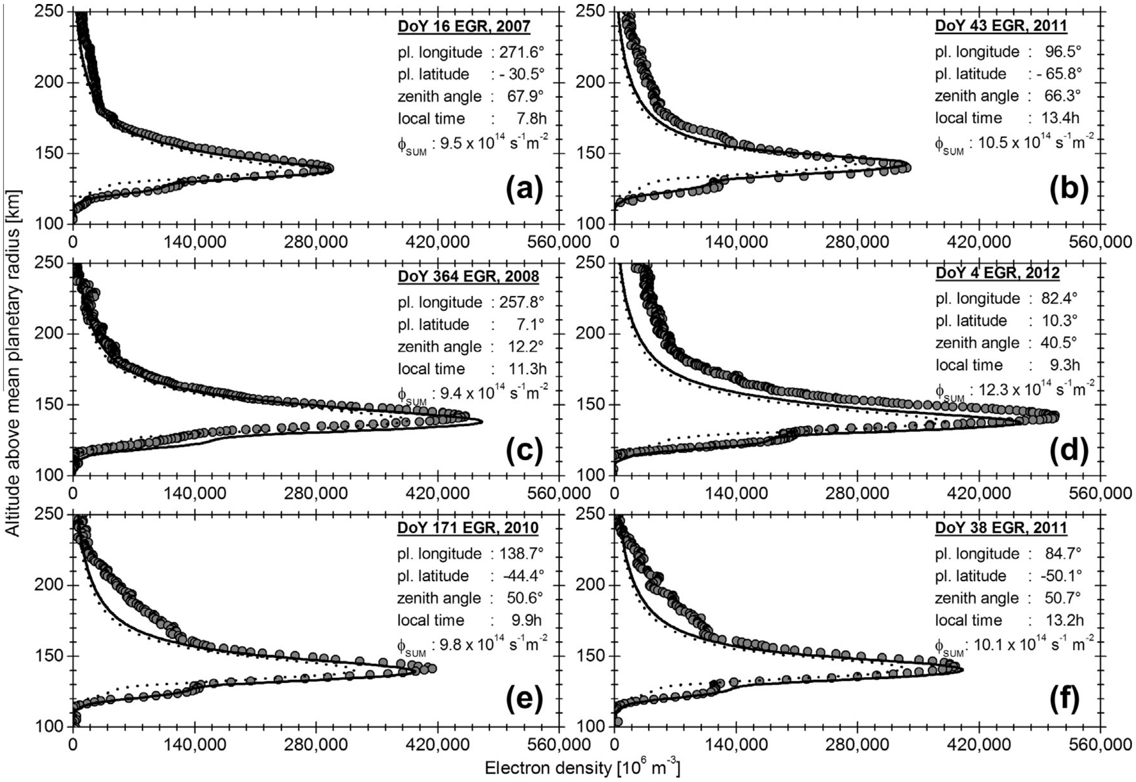

Fig. 11. Comparison between modeled and observed electron density profiles for the Venus ionosphere. Observation time and other parameters are given in the legend of each panel. Gray circles are the observed electron densities as a function of altitude relative to the mean planetary radius of 6051.8 km. The dotted lines are the modeled IonA profiles from photoionization only, using the VenusGRAM model as the neutral background atmosphere. The solid lines are modeled IonA profiles which consider additional secondary ionization.

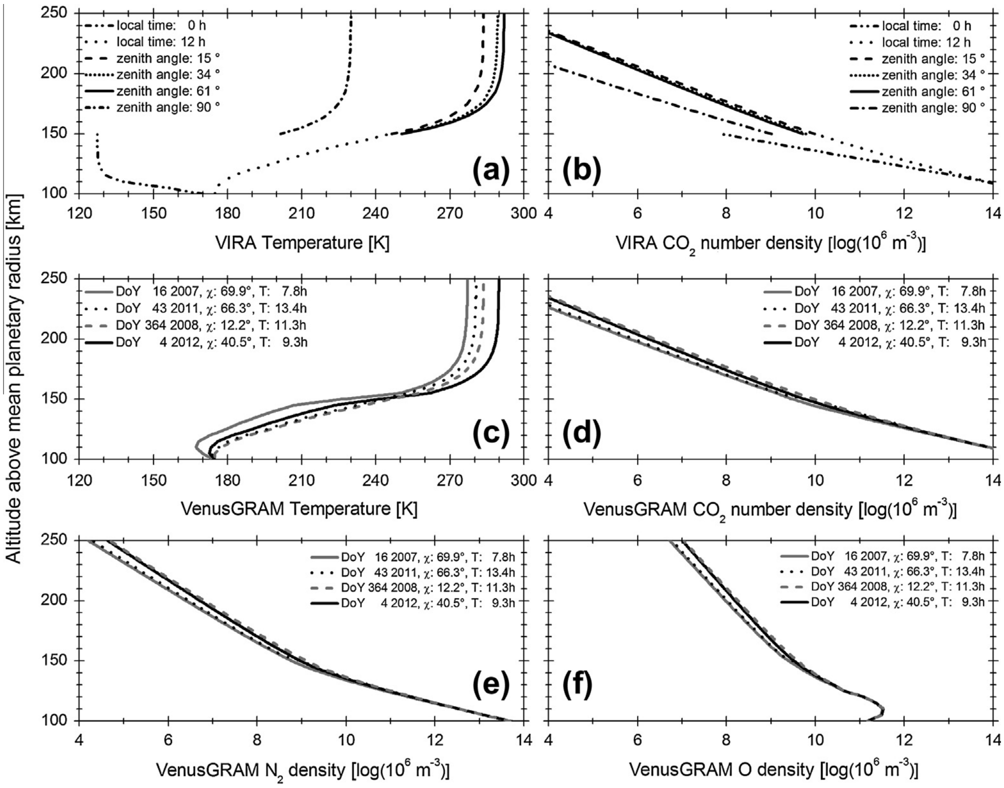

Fig. 12. (a and b) are VIRA (Kliore et al., 1985) temperature and number density profiles. From 100 to 150 km altitude, the only VIRA profiles available are for LT = 0 (midnight) and LT = 12 (noon). From 150 to 250 km altitude, the VIRA profiles depend on the solar zenith angle. VenusGRAM interpolates between the given profiles and bridges the transition region at 150 km altitude smoothly. (c–f) VenusGRAM profiles derived from the VIRA database for the observation parameters of the VeRa profiles in Fig. 11a–d (e, f are not shown for clarity).

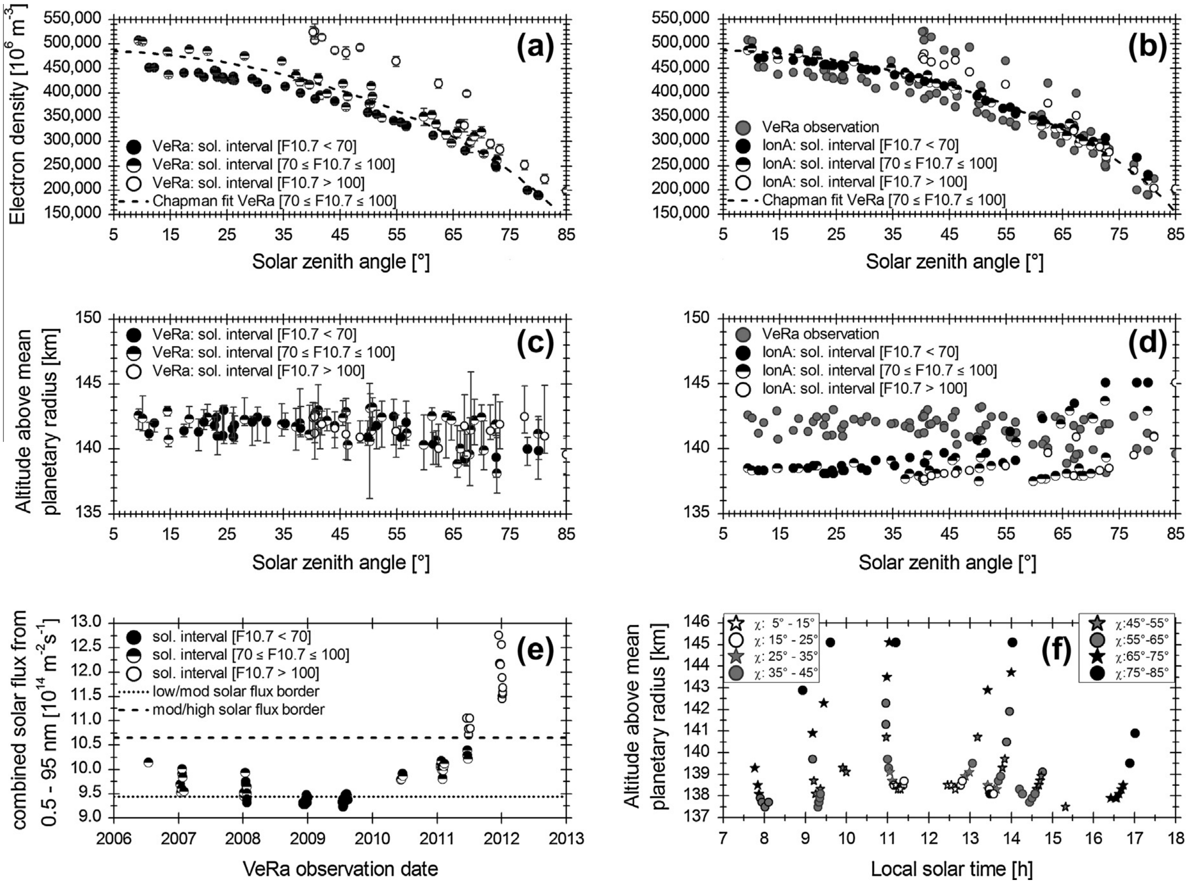

Fig. 13. (a) V2 peak density of the daytime ionospheric electron density profiles as a function of solar zenith angle. Three basis populations can be distinguished according to epoch as shown in panel (e): (i) low peak densities coinciding with time of low solar flux during solar minimum (black circles); (ii) low/medium peak densities (black/white circles) and high peak densities (white circles) coinciding with higher flux levels from the mid of 2011 to the beginning of 2012. The solid line is the fit of the Chapman relation with the fitting parameter $\varepsilon = 0.53 \pm 0.01$ to the $70 \leqslant F10.7 \leqslant 100$ solar interval data; (b) modeled V2 peak density compared to the VeRa observations from panel (a). The Chapman fit on the $70 \leqslant F10.7 \leqslant 100$ model data yields $\varepsilon = 0.48$; (c) V2 peak altitudes of VeRa observations; (d) comparison of modeled V2 peak altitudes to the observed values displayed in panel (c); (e) summed solar flux from 0.5 to 95 nm for every modeled observation as a function of observation time; (f) modeled V2 altitudes as a function of local time and solar zenith angle χ.

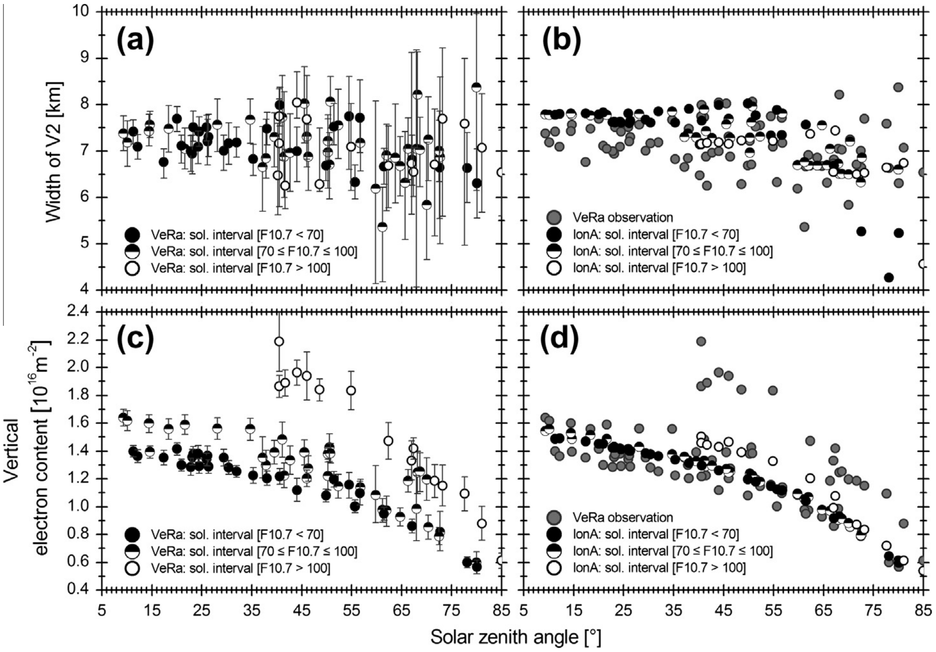

Fig. 14. (a) Observed V2 widths of the ionospheric main peak. Black circles indicate data from solar interval $F10.7 < 70$, black/white circles from solar interval $70 \leqslant F10.7 \leqslant 100$ and white circles from solar interval $F10.7 > 100$; (b) observed data (gray circles) and the IonA model results with the same color code as the observations in panel (a); (c) vertical total electron content (TEC) of the observed ionospheric profiles as a function of solar zenith angle and solar flux; (d) observed data compared to the IonA model results.

VIRA model. Fig. 13f shows the modeled V2 peak altitudes as a function of local solar time and solar zenith angle. As expected, the results are symmetric to the local solar time of 12 h. The V2 peak altitude for each solar zenith angle bin is highest around noon and drops for the morning and afternoon. For a given local solar time, the altitude of the peak increases with increasing solar zenith angle. This behavior is expected because of the 12 h symmetry of the VenusGRAM model atmosphere, but does not agree with the observations.

Fig. 14a shows the width of the observed V2 main peak. There is an increase in variance for higher solar zenith angles, but no obvious dependence on the solar flux. The modeled V2 widths are generally too broad (Fig. 14b) in comparison with the observations. There is a drop in the width of the V2 layer for solar zenith angles above 61°, which is caused by the discontinuity of the the VenusGRAM model at this solar zenith angle. This behavior does not agree with the observations. Fig. 14c shows the vertical electron content of the observed electron density profiles. The strong influence of the solar zenith angle and the solar flux on the observations can generally be reproduced by IonA (Fig. 14d), but it is not as pronounced as in the observations. While the observed TEC of the low solar flux data is overestimated in the model, the TEC for the high solar flux is underestimated. The best agreement between the observations and the model is found for the moderate solar flux $70 \leqslant \text{F10.7} \leqslant 100$.

The modeled V2 peak altitudes are systematically underestimated for $\chi < 45°$ (Fig. 13d). The altitude of the V2 layer is controlled by the neutral number density (and scale height). If the observed V2 peak altitude is higher than modeled with VIRA, then the true encountered neutral density distribution at ionospheric altitudes is also higher than predicted by VIRA. The width of the layer is controlled by the temperature. If the observed V2 width is smaller than modeled with VIRA, then the true encountered local temperature is smaller than predicted. Obviously, the true encountered atmosphere at ionospheric altitudes is denser but locally cooler than predicted by VIRA.

The next development step for the IonA software package is the inclusion of a simple 1D neutral atmospheric model for Venus. The underlying VenusGRAM neutral density and temperature profiles are to be varied in iterative steps until an agreement is achieved between the modeled and the observed electron density profile. This will allow the derivation of neutral density and temperature profiles at ionospheric heights for the time of the observation, thereby providing a possibility of improving the planned new neutral atmospheric VIRA model with VeRa data at ionospheric altitudes.

6. Conclusions

The IonA model is developed in order to compare observed and simulated ionospheric electron density profiles for actual observing conditions, e.g. solar flux, solar zenith angle, planetary coordinates and local time.

The modeling software uses models of neutral planetary atmospheres (MCD for Mars; VenusGRAM for Venus) as input, which define the number density, the distribution of neutral species and the temperature profile at ionospheric altitudes. The neutral species are ionized by solar radiation (X-ray to EUV continuum). Secondary ionization by impact ionization of photoelectrons is introduced by the W-model (Wedlund et al., 2011). We assume that the only loss process is the dissociative recombination of O_2^+. Transport effects are not yet included. The modeled electron number density as a function of altitude is compared with the observed electron density profile from the occultation.

For Mars, the observed decrease in M2 peak electron density with increasing solar zenith angle is reproduced with IonA for all five MCD scenarios. Observation and model show a clear increase of peak electron density for increasing solar flux at comparable solar zenith angles. No "best" MCD scenario could be found for the modeling of the M2 electron density, due to the higher variance in observed electron density, which is not reproduced by the IonA model. This is explained by observational uncertainties, model uncertainties because of missing plasma effects in the SOLAR2000/MCD databases and still lacking multidimensional and transport effects which are not yet included in IonA. The observed increase in the M2 peak altitude with increasing solar zenith angle is reproduced with all MCD scenarios. The same agreement is found for the observed increase in M2 peak altitude with solar flux for similar zenith angles. Best agreement for the M2 peak altitudes is achieved with the *low/clear* and *low/MY24* scenarios. The observed M2 width dependence on the solar zenith angle is different for the three defined solar flux intervals. A generally constant width for the $\text{F10.7} < 70$ interval in combination with decreasing solar flux indicates a slightly cooler atmosphere for the higher solar zenith angle observations. The M2 width for the $70 \leqslant \text{F10.7} \leqslant 100$ interval is increasing with solar zenith angle, as is the solar flux. Therefore an increase in H for higher solar zenith angles is caused by an increase in M2 altitude to higher scale height regions and a larger scale height caused by a generally warmer atmosphere induced by the larger solar flux. For the $\text{F10.7} > 100$ interval, the M2 width increases strongly with increasing solar zenith angle, while the solar flux is decreasing. The rising of the main peak up to altitudes with higher neutral scale heights is the main cause for the broadening of the M2 main layer. The modeled M2 width is generally broadening with increasing altitude, which is mainly caused by the overestimation of temperature and scale height in the MCD v4.3 scenarios. The observed total electron content decreases with increasing zenith angle, which is reproduced by all MCD scenarios, as is the observed strong relation of the observed TEC with the solar flux. Best agreement is found with the MCD *low/clear* and *low/MY24* scenarios.

On average, the MCD "low solar flux/clear atmosphere" (*low/clear*) and "low solar flux/Mars Year 24" (*low/MY24*) scenarios are best to reproduce the MaRS set of observations, although the encountered atmospheric temperature was still slightly cooler than predicted. Some individual MaRS observations are, however, in better agreement with other (warmer) MCD scenarios.

Evidence that the MCD overestimates the temperature at ionospheric altitudes is best seen in the comparison of modeled and observed M2 layer widths. The modeled layer widths are generally too broad. The width of the layer depends on the neutral scale height and therefore on the temperature of the neutral atmosphere. This confirms the results found by Forget et al. (2009) for a comparison of the MCD neutral atmosphere with SPICAM results. The SPICAM observations used by Forget et al. (2009) are mostly from the nightside atmosphere. The MaRS observations used in this paper are exclusively of dayside origin. Therefore, the comparison between MaRS observations and IonA model results on the basis of the MCD neutral atmosphere confirms the overestimate of temperatures at ionospheric altitudes for the dayside atmosphere of Mars. An improved version of the MCD will include a better description of the cooling produced by 15 μm emissions by CO_2 and its dependence with the abundance of atomic oxygen (López-Valverde et al., 2011). This cooling term, dominant at the upper mesosphere/lower thermosphere, has been identified as the likely cause of the overestimation of the temperatures (Forget et al., 2009; González-Galindo et al., 2009). Any improved MCD model will be incorporated into IonA as soon as it becomes publicly available.

IonA results for the Venus ionosphere are based on the VenusGRAM/VIRA neutral atmosphere model. It is concluded, that the VenusGRAM neutral atmosphere model can only be used in a very limited way for simulations and modeling of the observed electron density profiles at ionospheric altitudes. While the general solar zenith angle and solar flux dependence of the observed V2 peak electron density is reproduced by IonA, the modeled V2 peak electron densities are either overestimated or underestimated for low and high solar EUV fluxes, respectively. V2 peak densities modeled with medium solar fluxes barely match the observed peak densities for data in the solar interval $70 \leqslant$ F10.7 $\leqslant 100$. The modeled V2 peak altitudes are systematically underestimated by five kilometers on average for $\chi < 45°$. While the observed V2 peak altitudes decrease slightly for higher zenith angles, the model results show the opposite behavior for $\chi \geqslant 61°$. The model shows a symmetry about LT = 12 (noon), which is not found in the observations. There is an increase in variance for the observed V2 widths towards higher solar zenith angles, but no strong layer broadening or dependence on solar flux is found. Due to the VenusGRAM discontinuity at that zenith angle, the V2 model widths decrease strongly for solar zenith angles larger than 61°, a trend not visible in the observations. The observed TEC is largely influenced by the solar zenith angle and the available solar flux. The general trend for solar zenith angle and flux can be seen in the model results, but the observations for F10.7 < 70 are generally overestimated, while the observations for F10.7 > 100 generally underestimated. Although VIRA is valid for high solar activity (F10.7 = 150) there is generally very poor agreement with the few VeRa observations at solar maximum 2012.

Finally it can be said for all MaRs and VeRa observations, that the "bulge" feature could never be reproduced with the IonA model between the ionospheric main peak and the upper model border of 250 km altitude. It is concluded that the bulge must be of a more complex mechanism than actually modeled in IonA. Possible mechanisms are transport effects or the departure of the electron temperature T_e from the neutral temperature T_n in this altitude region.

The observed MaRS and VeRa electron density profiles, however, shall be used to improve the temperature and density profiles of the neutral background atmosphere at ionospheric altitudes. Additionally, the MaRS profiles could also be available to improve the next generation of the Mars Initial Reference Ionosphere – MIRI – (http://sirius.bu.edu/miri/index.php). Together with the comparison of the IonA ionospheric results with the MCD ionospheric model (González-Galindo et al., 2013) and the VIRA ionosphere (Bauer et al., 1985), these are the next development steps for the IonA model of the Mars and Venus ionospheres.

Acknowledgments

The Mars Express Radio Science Experiment (MaRS) and the Venus Express Radio Science Experiment (VeRa) are funded by the German Space Agency (DLR) under Grants 50QM1004 and 50OV1001. Support for Mars Express Radio Science at Stanford University is provided by NASA through JPL Contract 1217744. Support for the Multimission Radio Science Support Team is provided by NASA/JPL. Portions of this research were performed at the Jet Propulsion Laboratory, California Institute of Technology under contract with NASA. We thank everyone involved in the Mars Express and Venus Express projects at ESTEC, ESOC, ESAC, JPL, and the ESTRACK and DSN ground stations for their continuous support.

Solar Irradiance Platform historical irradiances are provided courtesy of W. Kent Tobiska and Space Environment Technologies. These historical irradiances have been developed with partial funding from the NASA UARS, TIMED, and SOHO missions.

We acknowledge support for work conducted on the development of the Mars Climate Database from the European Space Agency (under ESTEC Contract 11369/95/NL/JG(SC)) and from CNES. CNRS (LMD group), the IAA and the UK Particle Physics and Astronomy Research Council (AOPP, Oxford Group) also provided support during the development of the Martian General Circulation Models.

We thank the NAIF-team at JPL (headed by Charles Acton) for providing the SPICE software.

References

Avakyan, S.V., Il'in, R.N., Lavrov, V.M., Ogurtsov, G.N., 1998. Collision Processes and Excitation of UV Emission from Planetary Atmospheric Gases: A Handbook of Cross Sections. Gordon and Breach Science Publishers, Amsterdam and the Netherlands.

Bauer, S.J., Hantsch, M.H., 1989. Solar cycle variation of the upper atmosphere temperature of Mars. Geophys. Res. Lett. 16 (5), 373–376.

Bauer, S.J. et al., 1985. The Venus ionosphere. Adv. Space Res. 5 (11), 233–267.

Bertaux, J.-L. et al., 2004. SPICAM: Studying the global structure and composition of the martian atmosphere. In: Wilson, A. (Ed.), Mars Express, vol. 1240. ESA Publications Division, Noordwijk, pp. 95–120.

Bougher, S.W., Engel, S., Hinson, D.P., Forbes, J.M., 2001. Mars Global Surveyor radio science electron density profiles: Neutral atmosphere implications. Geophys. Res. Lett. 28 (16), 3091–3094.

Bougher, S.W., Engel, S., Hinson, D.P., Murphy, J.R., 2004. MGS Radio Science electron density profiles: Interannual variability and implications for the martian neutral atmosphere. J. Geophys. Res. 109 (E3).

Bougher, S.W., Blelly, P.-L., Combi, M., Fox, J.L., Mueller-Wodarg, I., Ridley, A., Roble, R.G., 2008. Neutral upper atmosphere and ionosphere modeling. Space Sci. Rev. 139, 107–141.

Brace, L., Kliore, A.J., 1991. The structure of the Venus ionosphere. Space Sci. Rev. 55 (1–4), 81–163.

Breus, T., Gringauz, K., Verigin, M.I., 1985. On the properties and origin of the Venus ionosphere. Adv. Space Res. 5 (9), 145–156.

Cravens, T.E., Kliore, A.J., Kozyra, J.U., Nagy, A.F., 1981. The ionospheric peak on the Venus dayside. J. Geophys. Res. 86 (A13), 11323–11329.

Duru, F., Gurnett, D.A., Frahm, R.A., Winningham, J.D., Morgan, D., Howes, G.G., 2009. Steep, transient density gradients in the martian ionosphere similar to the ionopause at Venus. J. Geophys. Res. 114 (A12).

Fjeldbo, G., Kliore, A.J., Eshleman, R., 1971. The neutral atmosphere of venus as studied with the Mariner V radio occultation experiments. The Astron. J. 76 (2), 123–140.

Forget, F. et al., 1999. Improved general circulation models of the martian atmosphere from the surface to above 80 km. J. Geophys. Res. 104 (E10), 24155–24175.

Forget, F. et al., 2009. Density and temperatures of the upper martian atmosphere measured by stellar occultations with Mars Express SPICAM. J. Geophys. Res. 114 (E1).

Fox, J.L., 2004. Response of the Martian thermosphere/ionosphere to enhanced fluxes of solar soft X rays. J. Geophys. Res. 109, A11310. http://dx.doi.org/10.1029/2004JA010380.

Fox, J.L., 2007. Near-terminator Venus ionosphere: How Chapman-esque? J. Geophys. Res. 112 (E4).

Fox, J.L., Zhou, P., Bougher, S.W., 1996. The martian thermosphere/ionosphere at high and low solar activities. Adv. Space Res. 17 (11), 203–218.

Fox, J.L., Kliore, A.J., 1997. Ionosphere: Solar cycle variations. In: Bougher, S.W. (Ed.), Venus II. The Univ. of Arizona Press, Tucson, pp. 161–188.

Fox, J.L., Sung, K.Y., 2001. Solar activity variations of the Venus thermosphere/ionosphere. J. Geophys. Res. 106 (A10), 21305–21335.

Fox, J.L., Yeager, K.E., 2006. Morphology of the near-terminator martian ionosphere: A comparison of models and data. J. Geophys. Res. 111 (A10309).

González-Galindo, F., Forget, F., López-Valverde, M.A., Angelats i Coll, M., Millour, E., 2009. A ground-to-exosphere martian general circulation model: 1. Seasonal, diurnal, and solar cycle variation of thermospheric temperatures. J. Geophys. Res. 114 (E4).

González-Galindo, F., Chaufray, J.-Y., López-Valverde, M.A., Gilli, G., Forget, F., Leblanc, F., Modolo, R., Hess, S., Yagi, M., 2013. Three-dimensional Martian ionosphere model: I. The photochemical ionosphere below 180 km. J. Geophys. Res.: Planets 118 (10), 2105–2123.

Haider, S.A. et al., 2009. D, E, and F layers in the daytime at high-latitude terminator ionosphere of Mars: Comparison with Earth's ionosphere using COSMIC data. J. Geophys. Res. 114 (A3).

Hanson, W.B., Mantas, G.P., 1988. Viking electron temperature measurements: Evidence for a magnetic field in the martian ionosphere. J. Geophys. Res. 93 (A7), 7538.

Hanson, W.B., Sanatani, S., Zuccaro, D.R., 1977. The martian ionosphere as observed by the Viking retarding potential analyzers. J. Geophys. Res. 82 (28), 4351–4363.

Häusler, B. et al., 2006. Radio science investigations by VeRa onboard the Venus Express spacecraft. Planet. Space Sci. 54 (13–14), 1315–1335.

Hinson, D.P., Simpson, R.A., Twicken, J.D., Tyler, G.L., 1999. Initial results from radio occultation measurements with Mars Global Surveyor. J. Geophys. Res. 104 (E11), 26997–27012.

Keating, G.M. et al., 1985. Models of Venus neutral upper atmosphere: Structure and composition. Adv. Space Res. 5 (11), 117–171.

Keating, G.M. et al., 1998. The structure of the upper atmosphere of Mars: In situ accelerometer measurements from Mars Global Surveyor. Science 279 (5357), 1672–1676.

Kliore, A.J., Mullen, L.F., 1989. The long-term behavior of the main peak of the dayside ionosphere of Venus during solar cycle 21 and its implications on the effect of the solar cycle upon the electron temperature in the main peak region. J. Geophys. Res. 94 (A10), 13339–13351.

Kliore, A.J., Levy, G.S., Cain, D.L., Fjeldbo, G., Rasool, S.I., 1967. Atmosphere and ionosphere of Venus from the Mariner V S-band radio occultation measurement. Science 158 (3809), 1683–1688.

Kliore, A.J., Woo, R., Armstrong, J.W., Patel, I.R., Croft, T.A., 1979. The polar ionosphere of Venus near the terminator from early Pioneer Venus Orbiter Radio Occultations. Science 203 (4382), 765–768.

Kliore, A.J., Moroz, V.I., Keating, G.M., 1985. The Venus international reference atmosphere. Adv. Space Res. 5 (11), 1–304.

Lemoine, F.G. et al., 2001. An improved solution of the gravity field of Mars (GMM-2B) from Mars Global Surveyor. J. Geophys. Res. 106 (E10), 23359–23376.

Lewis, S.R. et al., 1999. A climate database for Mars. J. Geophys. Res. 104 (E10), 24177–24194.

Liemohn, M.W., Dupre, A., Bougher, S.W., Trantham, M., Mitchell, D.L., Smith, M.D., 2012. Time-history influence of global dust storms on the upper atmosphere at Mars. Geophys. Res. Lett. 39 (11).

López-Valverde, M.A., González-Galindo, F., López-Puertas, M., 2011. Revisiting the radiative balance of the mesosphere of Mars. In: The Fourth International Workshop on the Mars Atmosphere: Modelling and Observation, 8–11 February, 2011, Paris, France.

Mahajan, K.K., Lodhi, N.K., Singh, S., 2009. Ionospheric effects of solar flares at Mars. Geophys. Res. Lett. 36, L15207. http://dx.doi.org/10.1029/2009GL039454.

Mariner Stanford Group, 1967. Venus: Ionosphere and atmosphere as measured by dual-frequency radio occultation of Mariner V. Science 158(3809), 1678–1683.

Martinis, C.R., Wilson, J.K., Mendillo, M.J., 2003. Modeling day-to-day ionospheric variability on Mars. J. Geophys. Res. 108 (A10), 1383.

Mendillo, M., Withers, P., Hinson, D.P., Rishbeth, H., Reinisch, B., 2006. Effects of solar flares on the ionosphere of Mars. Science 311 (5764), 1135–1138.

Mendillo, M., Lollo, A., Withers, P., Matta, M., Pätzold, M., Tellmann, S., 2011. Modeling Mars' ionosphere with constraints from same-day-observations by Mars Global Surveyor and Mars Express. J. Geophys. Res. 116, A11303. http://dx.doi.org/10.1029/2011JA016865.

Millour, E. et al., 2011. An improved Mars Climate Database. In: The 4th Intl. WS on Mars Atmosphere Modeling and Observations, Paris, 8–11 February 2011.

Molina-Cuberos, G.J., Witasse, O., Lebreton, J.-P., Rodrigo, R., López-Moreno, J.J., 2003. Meteoric ions in the atmosphere of Mars. Planet. Space Sci. 51 (3), 239–249.

Molina-Cuberos, G.J., López-Moreno, J.J., Arnold, F., 2008. Meteoric layers in planetary atmospheres. Space Sci. Rev. 137 (1–4), 175–191.

Pätzold, M. et al., 2004. MaRS: Mars Express Orbiter Radio Science. In: Wilson, A. (Ed.), Mars Express, vol. 1240. ESA Publications Division, Noordwijk, pp. 140–163.

Pätzold, M., Tellmann, S., Häusler, B., Hinson, D.P., Schaa, R., Tyler, G.L., 2005. A sporadic third layer in the ionosphere of Mars. Science 310, 837–839.

Pätzold, M. et al., 2007. The structure of Venus' middle atmosphere and ionosphere. Nature 450 (7170), 657–660.

Pätzold, M. et al., 2009a. MaRS: Mars Express Radio Science Experiment. In: Fletcher, K. (Ed.), Mars Express. ESA Communication Production Office, Noordwijk and the Netherlands, pp. 217–245.

Pätzold, M. et al., 2009b. A sporadic layer in the Venus lower ionosphere of meteoric origin. Geophys. Res. Lett. 36 (5), L05203.

Pesnell, W.D., Grebowsky, J., 2000. Meteoric magnesium ions in the martian atmosphere. J. Geophys. Res. 105 (E1), 1695–1707.

Peter, K., Pätzold, M., Häusler, B., Tellmann, S., Tyler, G.L., 2008. Ionopause features of Mars as observed by the radio science experiment MaRS on Mars Express. American Geophysical Union (Fall). Abstract #P13B-1319.

Rishbeth, H., Mendillo, M., 2004. Ionospheric layers of Mars and Earth. Planet. Space Sci. 52 (9), 849–852.

Schunk, R.W., Nagy, A.F., 2009. Ionospheres: Physics, Plasma Physics, and Chemistry, second ed. Cambridge Univ. Press, Cambridge and others.

Seidelmann, P.K. et al., 2002. Report of the IAU/IAG working group on cartographic coordinates and rotational elements of the planets and satellites: 2000. Celes. Mech. Dynam. Astron. 82 (1), 83–111.

Smith, F.L., Smith, C., 1972. Numerical evaluation of Chapman's grazing incidence integral $ch(X, \text{chi})$. J. Geophys. Res. 77 (19), 3592–3597.

Taylor, H.A., Brinton, H.C., Bauer, S.J., Hartle, R.E., Cloutier, P.A., Daniell, R.E., 1980. Global observations of the composition and dynamics of the ionosphere of Venus: Implications for the solar wind interaction. J. Geophys. Res. 85 (A13), 7765–7777.

Tellmann, S., Pätzold, M., Häusler, B., Bird, M.K., Tyler, G.L., 2009. Structure of the Venus neutral atmosphere as observed by the radio science experiment VeRa on Venus Express. J. Geophys. Res. 114, E00B36. http://dx.doi.org/10.1029/2008JE003204.

Tobiska, W.K. et al., 2000. The SOLAR2000 empirical solar irradiance model and forecast tool. J. Atmos. Solar-Terres. Phys. 62 (14), 1233–1250.

Wang, J.-S., Nielsen, E., 2003. Wavelike structures in the martian topside ionosphere observed by Mars Global Surveyor. J. Geophys. Res. 108 (E7).

Wedlund, S.C., Gronoff, G., Lilensten, J., Ménager, H., Barthélemy, M., 2011. Comprehensive calculation of the energy per ion pair or W values for five major planetary upper atmospheres. Ann. Geophys. 29 (1), 187–195.

Whalley, C.L., Plane, J.M.C., 2010. Meteoric ion layers in the martian atmosphere. Faraday Discuss. 147, 349–368.

Witasse, O., Nagy, A.F., 2006. Outstanding aeronomy problems at Venus. Planet. Space Sci. 54 (13–14), 1381–1388.

Witasse, O. et al., 2003. Effects of a dust storm on the coupled Mars thermosphere–ionosphere, EGS–AGU–EUG Joint Assembly, Abstracts Nice, France, 6–11 April 2003. Abstract #2192.

Withers, P., 2009. A review of observed variability in the dayside ionosphere of Mars. Adv. Space Res. 44 (3), 277–307.

Withers, P., Mendillo, M., 2005. Response of peak electron densities in the martian ionosphere to day-to-day changes in solar flux due to solar rotation. Planet. Space Sci. 53 (14–15), 1401–1418.

Withers, P., Bougher, S.W., Keating, G.M., 2003. The effects of topographically-controlled thermal tides in the martian upper atmosphere as seen by the MGS accelerometer. Icarus 164 (1), 14–32.

Withers, P., Mendillo, M., Hinson, D.P., Cahoy, K., 2008. Physical characteristics and occurrence rates of meteoric plasma layers detected in the martian ionosphere by the Mars Global Surveyor Radio Science Experiment. J. Geophys. Res. 113 (A12).

Withers, P. et al., 2012a. A clear view of the multifaceted dayside ionosphere of Mars. Geophys. Res. Lett. 39, L18202. http://dx.doi.org/10.1029/2012GL053193.

Withers, P. et al., 2012b. Observations of the nightside ionosphere of Mars by the Mars Express Radio Science Experiment (MaRS). J. Geophys. Res. 117 (A12).